Molecular layer deposition of zeolitic imidazolate framework-8 films

Reference:

Smets Jorid, Cruz Alexander John, Rubio-Gimenez Victor, Tietze Max L., Kravchenko Dmitry E., Arnauts Giel, Matavz Aleksander, Wauteraerts Nathalie, Tu Min, Marcoen Kristof, ...- Molecular layer deposition of zeolitic imidazolate framework-8 films
Chemistry of materials / American Chemical Society - ISSN 1520-5002 - Washington, Amer chemical soc, 35:4(2023), p. 1684-1690
Full text (Publisher's DOI): https://doi.org/10.1021/ACS.CHEMMATER.2C03439
To cite this reference: https://hdl.handle.net/10067/1952330151162165141

Molecular layer deposition of zeolitic imidazolate framework-8 films

Jorid Smets,[a,b,‡] Alexander John Cruz,[a,c,d,‡,†] Víctor Rubio-Giménez,[a] Max L. Tietze,[a] Dmitry E. Kravchenko,[a] Giel Arnauts,[a] Aleksander Matavž,[a] Nathalie Wauteraerts,[a] Min Tu,[a,§] Kristof Marcoen,[c] Inhar Imaz,[e] Daniel Maspoch,[e,g] Maxim Korytov,[d] Philippe M. Vereecken,[a,d] Steven De Feyter,[f] Tom Hauffman,[c] and Rob Ameloot[a,*]

[a] Center for Membrane Separations, Adsorption, Catalysis, and Spectroscopy (cMACS), KU Leuven - University of Leuven, Celestijnenlaan 200F, Leuven, 3001, Belgium

[b] Sustainable Energy, Air & Water Technology (DuEL), Department of Bioscience Engineering, University of Antwerp, Groenenborgerlaan 171, Antwerp, 2020, Belgium

[c] Research Group of Electrochemical and Surface Engineering, Department of Materials and Chemistry, Vrije Universiteit Brussel, Pleinlaan 2, Brussels, 1050, Belgium

[d] Imec, Kapeldreef 75, Leuven, 3001, Belgium

[e] Catalan Institute of Nanoscience and Nanotechnology (ICN2), CSIC and The Barcelona Institute of Science and Technology, Campus UAB, Bellaterra, Barcelona, 08193, Spain

[f] Department of Chemistry, Division of Molecular Imaging and Photonics, KU Leuven, Leuven, 3001, Belgium

[g] ICREA Pg. LluísCompanys23, Barcelona, 08010, Spain

ABSTRACT: Vapor-phase film deposition of metal-organic frameworks (MOFs) would facilitate the integration of these materials into electronic devices. We studied the vapor-phase layer-by-layer deposition of zeolitic imidazolate framework 8 (ZIF-8) by consecutive, self-saturating reactions of diethyl zinc, water, and 2-methylimidazole on a substrate. Two approaches were compared: (1) Direct ZIF-8 'molecular layer deposition' (MLD), which enables a nanometer-resolution thickness control and employs only self-saturating reactions, resulting in smooth films that are crystalline as-deposited, and (2) Two-step ZIF-8 MLD, in which crystallization occurs during a post-deposition treatment with additional linker vapor. The latter approach resulted in a reduced deposition time and an improved MOF quality, *i.e.*, increased crystallinity and probe molecule uptake, although the smoothness and thickness control were partially lost. Both approaches were developed in a modified atomic layer deposition reactor to ensure cleanroom compatibility.

Metal-organic frameworks (MOFs) are porous solids constructed from metal nodes connected by organic linkers. Because of their record specific surface areas, adsorption capacities, and dielectric/electronic properties, MOFs are of interest in catalysis,[1–4] gas storage,[5] molecular separations,[6,7] and electronic devices.[8–17] In electronics applications, conventional solvent-based synthesis methods may be disadvantageous due to corrosion, contamination, and surface tension effects.[13] In the absence of solvents and dissolved salts, these obstacles can be circumvented.[11,13,18–20] The MOF chemical vapor deposition (CVD) method, previously employed for the deposition of low-k dielectrics,[11] involves (1) the deposition of an oxide precursor layer followed by (2) exposure to linker vapor to form the MOF.[21] The conversion of the oxide layer into a porous MOF film results in a significant thickness expansion, often 10 × or more,[19,21–26] which makes thickness control in the nm-range challenging. Moreover, on some substrates, it is hard to obtain continuous MOF films below a critical metal oxide precursor thickness (e.g., < 3 nm for ZIF-8 growth on Si wafers).[27] For some applications, more precise control over the film thickness is desired.[19]

Molecular layer deposition (MLD) is based on consecutive, self-saturating surface reactions of vaporized precursors separated by inert gas purge streams.[28,29] The technique is closely related to atomic layer deposition (ALD) but uses at least one organic molecule as a building block. ALD is a staple in semiconductor processing, enabling coatings with excellent conformity, uniformity, and thickness control at the (sub-)nm-level.[30–32] Solution-based layer-by-layer deposition methods for MOFs based on alternatingly contacting a substrate with reactant solutions have been around for many years.[33,34] More recently, vapor-phase layer-by-layer deposition methods for MOFs have been reported (**Table S1**, **Figure 1a**).[20,28,35–44] Salmi *et al.* demonstrated MLD of MOF-5, and later expanded this technique to IRMOF-8.[35,36] Lausund and Nilsen reported MLD of UiO-66, and subsequently extended their approach to the amino-functionalized and expanded variants of this MOF.[38,39,45] Karpinnen *et al.* showed crystalline as-deposited copper-terephthalate via MLD.[44,46] These pioneering studies show the viability of MOF-MLD, even though, in most cases, crystalline materials were obtained only after a post-deposition treatment.[35,36,38,39,45,47] Apart from porous MOFs, **Table S1** lists several non-porous coordination polymers that have been deposited by MLD directly in crystalline form.[40,46,48] In 2019, Han *et al.* reported a vapor-phase layer-by-layer deposition of HKUST-1. In this study, metallic copper was evaporated rather than deposited in a self-limiting fashion. Films were crystalline as-deposited, though a limited thickness control was obtained (40 nm at 2 cycles).[41] In 2020, Silva *et al.* reported the MLD of an Eu-based UiO-66 analog. Though crystallinity was obtained in the as-deposited state, diffraction peaks were only observed after a high number of cycles (> 1000).[49]

Herein, we report the MLD of ZIF-8 thin films by consecutive self-saturating reactions of vaporized diethyl zinc (DEZ), water, and 2-methylimidazole (HmIM). We studied two different approaches: (1) Direct ZIF-8 MLD, in which crystallinity is obtained in the as-deposited state (**Figure 1b**), and (2) Two-step ZIF-8 MLD, in which the MOF crystallizes during a post-treatment step (**Figure 1c**).

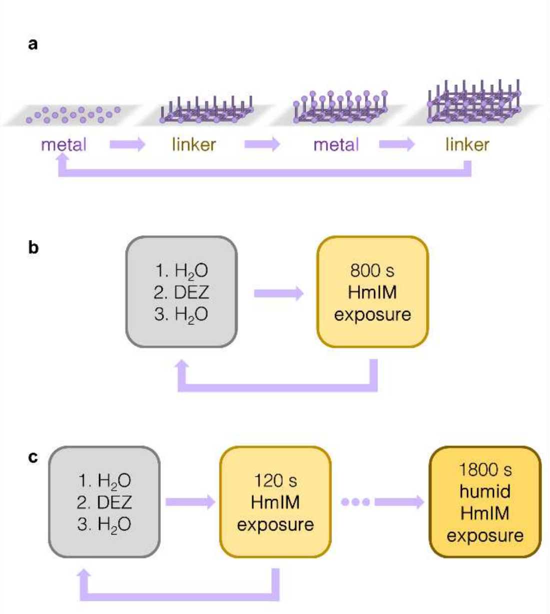

Figure 1. Schematic representation of ZIF-8 MLD. a) General representation of the vapor-phase layer-by-layer deposition. The protocols used for direct and two-step ZIF-8 MLD are shown in panels b and c, respectively.

Direct ZIF-8 MLD

An MLD protocol consists of reactant pulses separated by purge steps. In each cycle, sufficient reactant should be provided to complete the surface reaction. The purge steps should be long enough to remove all physisorbed (*i.e.*, non-reacted) precursor, though excessive purge steps will result in a lengthy process. In this work, a ZIF-8 MLD cycle comprises consecutively (1) deposition of a Zn-OH monolayer: first, H_2O pulses maximize the surface hydroxylation of the underlying layer to facilitate the reaction with the zinc precursor. Subsequently, DEZ pulses result in the deposition of a $\text{Zn-}C_2H_5$ monolayer. The next H_2O pulses remove the ethyl group, leaving a Zn-OH terminated surface. The formation of a Zn-OH monolayer is followed by (2) exposure to HmIM vapor to form ZIF-8. These steps are repeated to deposit a ZIF-8 film of a well-defined thickness at a growth rate of 9 Å/cycle. The crystallinity of the resulting films was confirmed by synchrotron grazing-incidence X-ray diffraction (GIXRD, **Figure 2a**), even for a single MLD cycle (**Figure S1**).

Ex-situ ellipsometry measurements of the deposited films after 10 cycles resulted in a modeled refractive index of 1.33 after activation at 100 °C in dynamic vacuum (λ = 633 nm), in line with values reported for ZIF-8 (1.30-1.38).[24,27,50] In addition, ellipsometry allows for monitoring the ZIF-8 MLD process *in-situ* and confirms the self-saturating behavior of the surface reactions (**Figure 2b,c**). In addition, these *in-situ* experiments revealed the relatively slow reaction kinetics and the need for a long HmIM pulse (800 s), even though the vapor pressure of HmIM is in the same order of magnitude as common ALD reactants (**Figure S2**).[51] For linker exposure times shorter than 400 s, no crystalline ZIF-8 films were obtained (**Figure S3**). Atomic force microscopy (AFM, **Figure 2d**) showed excellent surface coverage (RMS roughness 7.2 nm at 30 cycles), even at only three MLD cycles. The pinhole-free nature of the films was confirmed by conductive AFM measurements (**Figure S4**). If MOF-CVD was used instead, lower surface coverage was obtained for thin ZnO precursor layers (< 3 nm), as dispersed crystallites formed instead of a continuous film. This phenomenon can be explained by the increased mobility associated with longer linker exposure times (**Figure S5**).[22,27,52,53] The large-scale spatial uniformity of the ZIF-8 MLD films was verified by coating a 200 mm Si wafer with minimal thickness variation (29.5 ± 2.4 nm), as determined by *ex-situ* ellipsometry mapping, **Figure S6**.

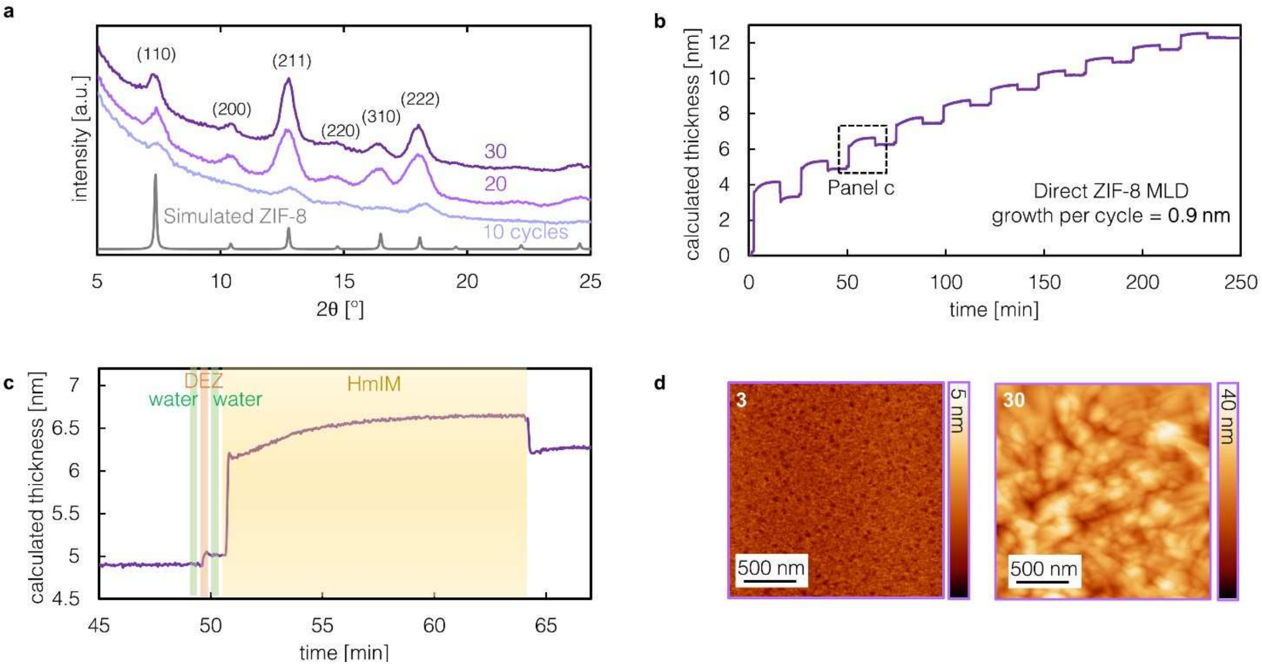

Figure 2. Direct ZIF-8 MLD a) Synchrotron GIXRD patterns for ZIF-8 films obtained through 10, 20, and 30 MLD cycles, compared to a simulated ZIF-8 diffractogram (CCDC code: VELVOY).[54] b) *In-situ* ellipsometry during direct ZIF-8 MLD deposition. Thickness from fitting the optical parameters of an extended Cauchy model after deposition, and using these constants to calculate the thickness as a function of time. The GPC is calculated starting from the third cycle to avoid deviations due to substrate interactions. c) Zoom of the *in-situ* ellipsometry data in panel (b). d) AFM measurements for 3 and 30 cycles of direct ZIF-8 MLD.

Water has multiple roles in the direct ZIF-8 MLD process: (1) generating Zn-OH moieties, resulting in a reactive surface, (2) protonating the linker,[55,56] hence rendering it susceptible to reaction with surface hydroxyls, and (3) promoting precursor mobility on the surface to aid crystallization.[57] Without a water pulse preceding the HmIM exposure, non-continuous ZIF-8 films were obtained due to the lower Zn-OH coverage (**Figure S7**). Removing both water pulses from the process resulted in amorphous films (**Figure S8**). Previous studies showed that CVD of ZIF-67, the Co^{2+}-equivalent of ZIF-8, is unsuccessful when water vapor is replaced by methanol or ethanol.[58,59] When the second water pulse in the ZIF-8 MLD process was replaced by methanol (*i.e.*, H_2O-DEZ-MeOH-HmIM), a crystalline yet rough and non-continuous ZIF-8 film was obtained (**Figure S9**, RMS roughness of 10.3 nm at 30 cycles) as the surface was covered with $Zn-O-CH_3$ and $Zn-C_2H_5$ instead of Zn-OH.[60] When both water pulses were replaced by methanol (*i.e.*, MeOH-DEZ-MeOH-HmIM), no crystalline ZIF-8 was formed (**Figure S9**).

Ellipsometric porosimetry using methanol as a probe molecule was used to evaluate the uptake properties of the ZIF-8 MLD films. These measurements indicate that, even though the ZIF-8 MLD films have crystalline domains, they are likely highly defective. Compared to solution-deposited films, the MLD films showed a much lower uptake, and the methanol isotherms lack the characteristic S-shape (**Figure S10b**), likely because of an abundance of Zn-OH defects. We found that the adsorption behavior of the films could be much improved through a post-deposition treatment step with humid HmIM vapor (1800 s), resulting in an increased methanol adsorption capacity and S-shaped isotherm (**Figure S10**). In contrast, only minor improvements in the crystallinity were observed (**Figure 3a**). We hypothesize that the post-treatment heals surface defects, thus improving the pore accessibility.

Two-step MOF-MLD

The direct MLD method is impractically slow (10 cycles take 4 h). Therefore, we tested a two-step ZIF-8 MLD approach (**Figure 1c)** with a much shorter linker exposure step during film growth (120 instead of 500 s) and reduced purge times (180 instead of 500 s) followed by post-deposition treatment with humid HmIM vapor. Since HmIM vapor pressure builds up slowly in in the linker canister, the linker concentration in the carrier gas is reduced when purging is shortened to 180 s. During the deposition stage, a non-crystalline film with the same composition as ZIF-8 is deposited at a rate of 6 Å/cycle (**Figure 3b**); crystallization occurs during the subsequent humid HmIM exposure. After the post-deposition treatment, a modeled thickness of around 27

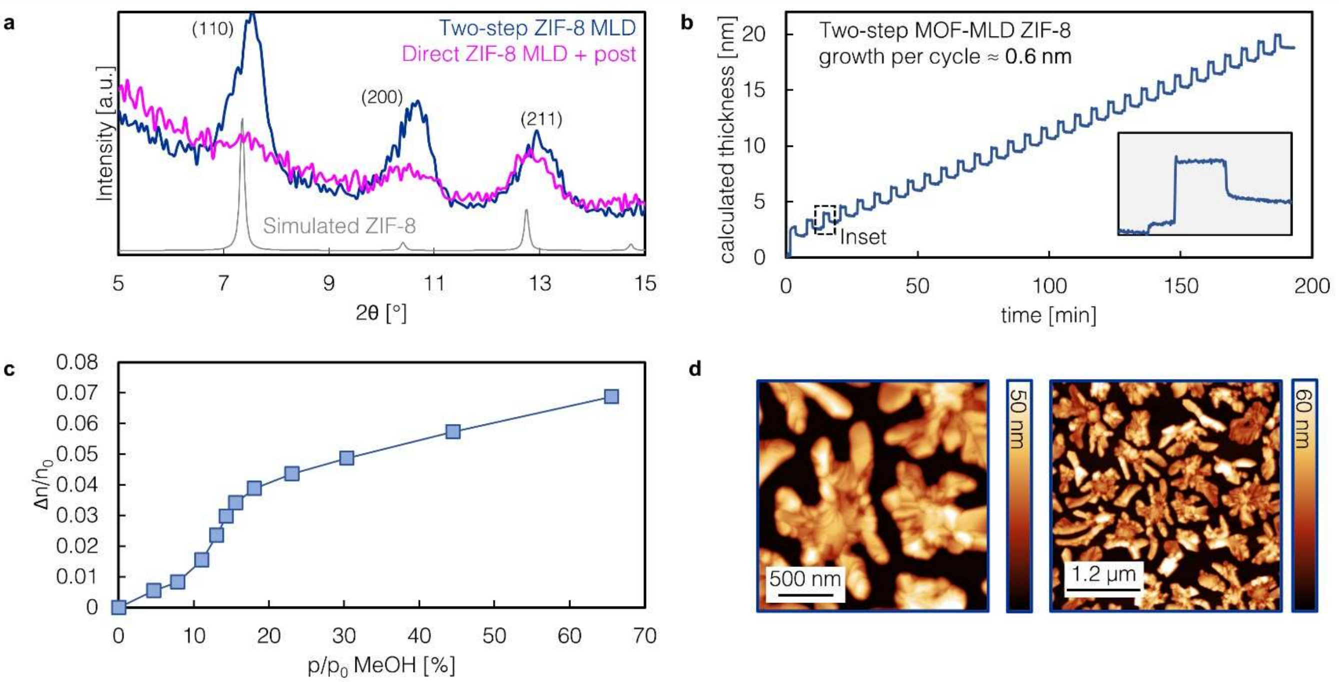

Figure 3. Two-step ZIF-8 MLD a) GIXRD comparing two-step ZIF-8 MLD (blue), and post-treated direct ZIF-8 MLD (pink). Both samples consist of 30 MLD cycles. b) *In-situ* ellipsometry during direct ZIF-8 MLD deposition, modelled as a Cauchy layer. Inset: 7-min time window. c) Ellipsometric porosimetry, modelled with an extended Cauchy model d) AFM of two-step ZIF-8 MLD on Si wafer.

nm is obtained (n is ~1.30 at 633 nm). The crystallinity (**Figure 3a**) and methanol adsorption capacity (**Figure 3c, S10c**) measured for these films were higher compared to films obtained through direct ZIF-8 MLD, even after post-deposition treatment: $\Delta n_{65.58\%}/n_o$(direct) = 0.013; $\Delta n_{65.58\%}/n_o$(direct + post) = 0.048, and $\Delta n_{65.58\%}/n_o$(two-step) = 0.069.

Hard X-ray photoelectron spectroscopy (HAXPES) using Ga K_α radiation was employed to study the ZIF-8 film properties because of the much larger inelastic mean free path length compared to Al K_α in XPS.[61] Therefore, HAXPES probes bulk rather than surface properties of nanometric films. HAXPES measurements show a N/Zn ratio of 3.6 for two-step ZIF-8 MLD, which is closer the ideal N/Zn of 4 than direct ZIF-8 MLD (N/Zn = 3.2), *i.e.*, there are fewer missing linkers in the framework (**Figure S11, S12**). Nevertheless, a defect sub-peak must be fitted when modeling the zinc and nitrogen peaks.[24] The defect fraction, defined as the intensity of the defect sub-peak relative to the total peak intensity, is higher for direct ZIF-8 MLD ($Zn_{defect}/Zn_{ZIF\text{-}8}+Zn_{defect}$ = 0.14, $N_{defect}/N_{ZIF\text{-}8}+N_{defect}$ = 0.14) than for two-step ZIF-8 MLD ($Zn_{defect}/Zn_{ZIF\text{-}8}+Zn_{defect}$ = 0.08, $N_{defect}/N_{ZIF\text{-}8}+N_{defect}$ = 0.06, **Figure S12**). Still, after storage in ambient air at room temperature for a few weeks, the crystallinity of the two-step MLD film dropped, and the methanol uptake and its characteristic isotherm shape disappeared (**Figure S13**). Degradation likely occurs through hydrolysis of the N-Zn bond and is faster for more defective films.

Mobility during HmIM exposure

For both direct ZIF-8 MLD and two-step ZIF-8 MLD, the HmIM post-deposition treatment improved the adsorption properties, but resulted in increased roughness due to Ostwald ripening (**Figure 3d, S10d,** RMS roughness 15.9 and 16.1 nm for direct MLD and two-step MLD after post-treatment, respectively). The fact that HmIM vapor exposure induces mobility in an existing ZIF layer could complicate the fabrication of MOF-on-MOF structures. These layered structures are recently gaining interest,[62] therefore to study this effect and assess the viability of depositions on existing ZIF frameworks, depositions were performed on (100)-oriented ZIF-8 supercrystals (**Figure S14a**).[63] Specular XRD was used to calculate the degree of crystallographic orientation as the peak intensity ratio of the (200) and (110) reflections. Due to the very low intensity of the (110) reflection for the oriented supercrystals, slight intensity changes in this peak will result in a significant variation of the (200)/(110) ratio. Therefore, this number is extremely sensitive to loss in crystalline orientation. Direct ZIF-8 MLD without a post-treatment step was used to avoid recrystallization of the supercrystal substrate. By depositing on an existing ZIF-8 framework (as with seeded growth methods), the local energetic barrier for crystal nucleation is lowered,[13] and the direct

MLD film quality is improved. When ZIF-8 CVD is performed on top of these crystals as a comparison, we observe that the crystalline orientation is lost due to recrystallization into a randomly oriented ZIF-8 (**Figure S14**). When direct ZIF-8 MLD is used, more of the orientation of the underlying substrate is maintained, though a decreasing trend with an increasing number of cycles is observed. To further characterize ZIF-8 MLD depositions on existing frameworks, conformality of the MOF-on-MOF coating was verified *via* SEM-EDX mapping of a ZIF-67 analog of the supercrystal substrate after MLD (**Figure S15-16**).

Conclusion

We show two approaches for ZIF-8 MLD, namely a direct method with nanometer-resolution thickness control where crystallinity is observed in the as-deposited state and a more practical two-step process that yields a higher MOF quality at a significantly shorter deposition time. These protocols expand the vapor-phase MOF deposition methods. We believe that MOF-MLD could be developed for all materials that can be deposited via MOF-CVD if there is an ALD precursor available to supply the metal without the need for strongly oxidizing co-reactants.

Methods

ZIF-8 MOF-MLD: The MOF-MLD ZIF-8 layers were deposited using deionized water (DIW), diethylzinc (DEZ, 97%, STREM), and freshly-ground HmIM (30 g, 99%, Sigma Aldrich) as precursors. Nitrogen (99.999%) was the carrier and purging gas used and sourced from a cleanroom header. Three 0.015 s pulses of DEZ in between two sets of three 0.015 s pulses of water were first dosed, separated by a purge duration of 5 s. This step was followed by HmIM exposure at stopped-flow conditions. In this step, the N_2 flow was stopped, and the outlet valve was closed, with an N_2 bubbler pressure of 110 mbar. As detailed in our previous work,[27] the bubbler-type sublimation vessel, supplied with 30 g of HmIM, was set to 125 °C, while the outlet and supply lines and the connections to the MOF reactor chamber were fixed to 130 °C and 135 °C, respectively. These lines were progressively heated in 30-minute intervals to prevent clogging during start-up. Before the depositions, purging and drying sequences (100 °C, 30 min) were implemented to ensure the removal of air in the headspace of the bottle and moisture/adsorbed water in the HmIM powder bed. The reactor base pressure during deposition was ~ 0.40 mbar at an N_2 gas flow of 20 sccm (manifold temperature: 150 °C). All depositions were carried out in a modified Savannah S-200 thermal ALD reactor (Veeco Instruments, Inc.) in an ISO 6 cleanroom (21 ± 1°C, relative humidity: 40 ± 5%). The different protocols mentioned in the main text (*i.e.*, direct MOF-MLD and two-step MOF-MLD) are schematically shown in **Figure S17** and **S18**. In all studied protocols, the importance of the thermal gradient in the reactor chamber has proven to be indispensable. The absence of or a diminished gradient resulted in an unsuccessful generation of ZIF-8 (**Figure S19**, **S20**).

Humidified conditions linker exposure: Immediately before dosing HmIM, ten additional water pulses were introduced in stopped-flow conditions, resulting in ~12% relative humidity (RH) in the reactor. This RH value was estimated by noting the pressure increase in the chamber after dosing, divided by the water saturation pressure at the reactor chamber temperature (80 °C).

MOF Activation protocol: The MLD recipes were terminated with an activation step. For this purpose, the N_2 flow was increased from 10 to 200 sccm. The vacuum was kept at 8.5 mbar as the substrate temperature was ramped up to 100ºC and kept at this temperature. Since *in-situ* ellipsometry showed a constant profile after ~15 min (**Figure S21**), the activation sequence was terminated after 30 min.

ASSOCIATED CONTENT

The Supporting Information is available free of charge on the ACS Publications website:

> Methods section (cont.); vapor-phase LBL deposition of MOFs in literature; synchrotron GIXRD at low number of cycles, Knudsen effusion measurements; effect of linker exposure time; c-AFM shows pinhole-free films; AFM of MOF-CVD with thin ZnO precursor layer; full-wafer ellipsometry mapping; direct ZIF-8 MLD with missing water pulse(s); (partially) substituting water with methanol; humidified conditions post-treatment of direct ZIF-8 MLD; HAXPES measurements; sample aging in lab air; deposition of oriented supercrystals; graphical illustration of direct and two-step ZIF-8 MLD protocols; need for a thermal gradient in the reactor chamber; ellipsometry during activation step; and ellipsometric porosimetry as a function of time (PDF)

AUTHOR INFORMATION

Corresponding Author

* E-mail: rob.ameloot@kuleuven.be

Present Addresses

† Baker Hughes, Schumanplein 6, Brussels 1040 Belgium
§ 2020 X-Lab and State Key Laboratory of Transducer Technology, Shanghai Institute of Microsystem and Information Technology, Chinese Academy of Sciences, Shanghai 200050, China

Author Contributions

‡ These authors contributed equally.

Notes

The authors declare no conflict of interest.

ACKNOWLEDGMENT

This project has received funding from the European Research Council (ERC) under the European Union's Horizon 2020 research and innovation program (grant agreement n° 716472, acronym VAPORE), from the Research Foundation Flanders (FWO Vlaanderen) in projects G085720N and G087422N, from VLAIO in project HBC.2020.2612, and from KU Leuven in project C14/20/085. The FWO Vlaanderen large-infrastructure project: HERCULES HAXPES (I014018N) is acknowledged. ICN2 is supported by the Severo Ochoa program from the Spanish MINECO (grant SEV-2017-0706). J.S., V.R.-G., G.A., M.T., N.W, and T.H. acknowledge the support of the FWO Vlaanderen for respectively the following fellowships: 11H8121N, 1263622N, 1SA7320N, 12ZK720N, 1SB7921N and 1295317N. D.E.K. acknowledges the Marie Sklodowska Curie Training Network HYCOAT, Grant Agreement 765378, for the financial support. The authors want to thank Mikhail Krishtab, Margot Verstreken, Sabina Rodríguez-Hermida, Michel De Cooman, Sammy W. Verbruggen, and Ivo Stassen for fruitful discussions. We gratefully acknowledge DELTA Dortmund synchrotron for the allocation of beamtime at beamline BL9 (proposal n° ID77) under the guidance of Christian Sternemann and Michael Paulus. We acknowledge Elettra Syncrotrone Trieste for providing access to its synchrotron radiation facilities (proposal n° 20180092, 20190028, 20200226, and 20210060) and thank Luisa Barba and Nicola Demitri for assistance in using beamline XRD1. The research leading to this result has been supported by the project CALIPSOplus under Grant Agreement 730872 from the EU Framework Programme for Research and Innovation HORIZON 2020.

ABBREVIATIONS

MOF, Metal-organic framework; MLD, Molecular layer deposition; ZIF, Zeolitic imidazolate framework; HmIM, 2-methyl imidazolate; DEZ, Diethyl zinc; CVD, Chemical vapor deposition; ALD, Atomic layer deposition; GPC, Growth per cycle; GIXRD, Grazing incidence X-ray diffraction; AFM, Atomic force microscopy; RMS, Root mean squared; HAXPES, Hard X-ray photoelectron spectroscopy; SEM-EDX, Scanning electron microscopy with energy dispersive x-ray analysis.

REFERENCES

(1) Lee, J.; Farha, O. K.; Roberts, J.; Scheidt, K. A.; Nguyen, S. T.; Hupp, J. T. Metal–Organic Framework Materials as Catalysts. *Chem. Soc. Rev.* **2009**, *38* (5), 1450–1459. https://doi.org/10.1039/B807080F.

(2) Furukawa, H.; Cordova, K. E.; O'Keeffe, M.; Yaghi, O. M. The Chemistry and Applications of Metal-Organic Frameworks. *Science* **2013**, *341* (6149), 1230444. https://doi.org/10.1126/science.1230444.

(3) Mueller, U.; Schubert, M.; Teich, F.; Puetter, H.; Schierle-Arndt, K.; Pastré, J. Metal–Organic Frameworks—Prospective Industrial Applications. *J. Mater. Chem.* **2006**, *16* (7), 626–636. https://doi.org/10.1039/B511962F.

(4) Czaja, A. U.; Trukhan, N.; Müller, U. Industrial Applications of Metal–Organic Frameworks. *Chem. Soc. Rev.* **2009**, *38* (5), 1284–1293. https://doi.org/10.1039/B804680H.

(5) Ma, S.; Zhou, H.-C. Gas Storage in Porous Metal-Organic Frameworks for Clean Energy Applications. *Chem. Commun.* **2010**, *46* (1), 44–53. https://doi.org/10.1039/B916295J.

(6) Li, X.; Liu, Y.; Wang, J.; Gascon, J.; Li, J.; Bruggen, B. V. der. Metal–Organic Frameworks Based Membranes for Liquid Separation. *Chem. Soc. Rev.* **2017**, *46* (23), 7124–7144. https://doi.org/10.1039/C7CS00575J.

(7) Ma, X.; Kumar, P.; Mittal, N.; Khlyustova, A.; Daoutidis, P.; Mkhoyan, K. A.; Tsapatsis, M. Zeolitic Imidazolate Framework Membranes Made by Ligand-Induced Permselectivation. *Science* **2018**, *361* (6406), 1008–1011. https://doi.org/10.1126/science.aat4123.

(8) Bétard, A.; Fischer, R. A. Metal–Organic Framework Thin Films: From Fundamentals to Applications. *Chem. Rev.* **2012**, *112* (2), 1055–1083. https://doi.org/10.1021/cr200167v.

(9) Kirchon, A.; Feng, L.; Drake, H. F.; Joseph, E. A.; Zhou, H.-C. From Fundamentals to Applications: A Toolbox for Robust and Multifunctional MOF Materials. *Chem. Soc. Rev.* **2018**, *47* (23), 8611–8638. https://doi.org/10.1039/C8CS00688A.

(10) Yoon, S. M.; Warren, S. C.; Grzybowski, B. A. Storage of Electrical Information in Metal–Organic-Framework Memristors. *Angew. Chem.* **2014**, *126* (17), 4526–4530. https://doi.org/10.1002/ange.201309642.

(11) Krishtab, M.; Stassen, I.; Stassin, T.; Cruz, A. J.; Okudur, O. O.; Armini, S.; Wilson, C.; De Gendt, S.; Ameloot, R. Vapor-Deposited Zeolitic Imidazolate Frameworks as Gap-Filling Ultra-Low-k Dielectrics. *Nat. Commun.* **2019**, *10* (1), 3729. https://doi.org/10.1038/s41467-019-11703-x.

(12) Talin, A. A.; Centrone, A.; Ford, A. C.; Foster, M. E.; Stavila, V.; Haney, P.; Kinney, R. A.; Szalai, V.; Gabaly, F. E.; Yoon, H. P.; Léonard, F.; Allendorf, M. D. Tunable Electrical Conductivity in Metal-Organic Framework Thin-Film Devices. *Science* **2014**, *343* (6166), 66–69. https://doi.org/10.1126/science.1246738.

(13) Stassen, I.; Burtch, N.; Talin, A.; Falcaro, P.; Allendorf, M.; Ameloot, R. An Updated Roadmap for the Integration of Metal–Organic Frameworks with Electronic Devices and Chemical Sensors. *Chem. Soc. Rev.* **2017**, *46* (11), 3185–3241. https://doi.org/10.1039/C7CS00122C.

(14) Tu, M.; Xia, B.; Kravchenko, D. E.; Tietze, M. L.; Cruz, A. J.; Stassen, I.; Hauffman, T.; Teyssandier, J.; De Feyter, S.; Wang, Z.; Fischer, R. A.; Marmiroli, B.; Amenitsch, H.; Torvisco, A.; Velásquez-Hernández, M. de J.; Falcaro, P.; Ameloot, R. Direct X-Ray and Electron-Beam Lithography of Halogenated Zeolitic Imidazolate Frameworks. *Nat. Mater.* **2021**, *20* (1), 93–99. https://doi.org/10.1038/s41563-020-00827-x.

(15) Allendorf, M. D.; Schwartzberg, A.; Stavila, V.; Talin, A. A. A Roadmap to Implementing Metal-Organic Frameworks in Electronic Devices: Challenges and Critical Directions. *Chemistry – Chem. Eur. J.* **2011**, *17* (41), 11372–11388. https://doi.org/10.1002/chem.201101595.

(16) Allendorf, M. D.; Dong, R.; Feng, X.; Kaskel, S.; Matoga, D.; Stavila, V. Electronic Devices Using Open Framework Materials. *Chem. Rev.* **2020**, *120* (16), 8581–8640. https://doi.org/10.1021/acs.chemrev.0c00033.

(17) Rubio-Giménez, V.; Tatay, S.; Martí-Gastaldo, C. Electrical Conductivity and Magnetic Bistability in Metal–Organic Frameworks and Coordination Polymers: Charge Transport and Spin Crossover at the Nanoscale. *Chem. Soc. Rev.* **2020**, *49* (15), 5601–5638. https://doi.org/10.1039/C9CS00594C.

(18) Friščić, T.; Halasz, I.; Beldon, P. J.; Belenguer, A. M.; Adams, F.; Kimber, S. A. J.; Honkimäki, V.; Dinnebier, R. E. Real-Time and in Situ Monitoring of Mechanochemical Milling Reac-

tions. *Nat. Chem.* **2013**, *5* (1), 66–73. https://doi.org/10.1038/nchem.1505.

(19) Su, P.; Tu, M.; Ameloot, R.; Li, W. Vapor-Phase Processing of Metal–Organic Frameworks. *Acc. Chem. Res.* **2022**, 55 (2), 186–196. https://doi.org/10.1021/acs.accounts.1c00600.

(20) Crivello, C.; Sevim, S.; Graniel, O.; Franco, C.; Pané, S.; Puigmartí-Luis, J.; Muñoz-Rojas, D. Advanced Technologies for the Fabrication of MOF Thin Films. *Mater. Horiz.* **2020**, 10.1039.D0MH00898B. https://doi.org/10.1039/D0MH00898B.

(21) Stassen, I.; Styles, M.; Grenci, G.; Gorp, H. V.; Vanderlinden, W.; Feyter, S. D.; Falcaro, P.; Vos, D. D.; Vereecken, P.; Ameloot, R. Chemical Vapour Deposition of Zeolitic Imidazolate Framework Thin Films. *Nat. Mater.* **2016**, *15* (3), 304–310. https://doi.org/10.1038/nmat4509.

(22) Stassin, T.; Stassen, I.; Marreiros, J.; Cruz, A. J.; Verbeke, R.; Tu, M.; Reinsch, H.; Dickmann, M.; Egger, W.; Vankelecom, I. F. J.; De Vos, D. E.; Ameloot, R. Solvent-Free Powder Synthesis and MOF-CVD Thin Films of the Large-Pore Metal–Organic Framework MAF-6. *Chem. Mater.* **2020**, *32* (5), 1784–1793. https://doi.org/10.1021/acs.chemmater.9b03807.

(23) Stassin, T.; Stassen, I.; Wauteraerts, N.; Cruz, A. J.; Kräuter, M.; Coclite, A. M.; De Vos, D.; Ameloot, R. Solvent-Free Powder Synthesis and Thin Film Chemical Vapor Deposition of a Zinc Bipyridyl-Triazolate Framework. *EurJIC* **2020**, *2020* (1), 71–74. https://doi.org/10.1002/ejic.201901051.

(24) Tietze, M. L.; Obst, M.; Arnauts, G.; Wauteraerts, N.; Rodríguez-Hermida, S.; Ameloot, R. Parts-per-Million Detection of Volatile Organic Compounds via Surface Plasmon Polaritons and Nanometer-Thick Metal–Organic Framework Films. *ACS Appl. Nano Mater.* **2022**, acsanm.2c00012. https://doi.org/10.1021/acsanm.2c00012.

(25) Tu, M.; Kravchenko, D. E.; Xia, B.; Rubio-Giménez, V.; Wauteraerts, N.; Verbeke, R.; Vankelecom, I. F. J.; Stassin, T.; Egger, W.; Dickmann, M.; Amenitsch, H.; Ameloot, R. Template-Mediated Control over Polymorphism in the Vapor-Assisted Formation of Zeolitic Imidazolate Framework Powders and Films. *Angew. Chem., Int. Ed.* **2021**, *60* (14), 7553–7558. https://doi.org/10.1002/anie.202014791.

(26) Rubio-Giménez, V.; Arnauts, G.; Wang, M.; Oliveros Mata, E. S.; Huang, X.; Lan, T.; Tietze, M. L.; Kravchenko, D. E.; Smets, J.; Wauteraerts, N.; Khadiev, A.; Novikov, D. V.; Makarov, D.; Dong, R.; Ameloot, R. Chemical Vapor Deposition and High-Resolution Patterning of a Highly Conductive Two-Dimensional Coordination Polymer Film. *J. Am. Chem. Soc.* **2023**, *145* (1), 152–159. https://doi.org/10.1021/jacs.2c09007.

(27) Cruz, A. J.; Stassen, I.; Krishtab, M.; Marcoen, K.; Stassin, T.; Rodríguez-Hermida, S.; Teyssandier, J.; Pletincx, S.; Verbeke, R.; Rubio-Giménez, V.; Tatay, S.; Martí-Gastaldo, C.; Meersschaut, J.; Vereecken, P. M.; De Feyter, S.; Hauffman, T.; Ameloot, R. Integrated Cleanroom Process for the Vapor-Phase Deposition of Large-Area Zeolitic Imidazolate Framework Thin Films. *Chem. Mater.* **2019**, *31* (22), 9462–9471. https://doi.org/10.1021/acs.chemmater.9b03435.

(28) Ahvenniemi, E.; Karppinen, M. *In Situ* Atomic/Molecular Layer-by-Layer Deposition of Inorganic-Organic Coordination Network Thin Films from Gaseous Precursors. *Chem. Mater.* **2016**, *28* (17), 6260–6265. https://doi.org/10.1021/acs.chemmater.6b02496.

(29) Sundberg, P.; Karppinen, M. Organic and Inorganic–Organic Thin Film Structures by Molecular Layer Deposition: A Review. *Beilstein J. Nanotechnol.* **2014**, 5 (1), 1104–1136. https://doi.org/10.3762/bjnano.5.123.

(30) Elam, J. W.; Routkevitch, D.; Mardilovich, P. P.; George, S. M. Conformal Coating on Ultrahigh-Aspect-Ratio Nanopores of Anodic Alumina by Atomic Layer Deposition. *Chem. Mater.* **2003**, *15* (18), 3507–3517. https://doi.org/10.1021/cm0303080.

(31) Meng, X. An Overview of Molecular Layer Deposition for Organic and Organic–Inorganic Hybrid Materials: Mechanisms, Growth Characteristics, and Promising Applications. *J. Mater. Chem. A* **2017**, 5 (35), 18326–18378. https://doi.org/10.1039/C7TA04449F.

(32) Johnson, R. W.; Hultqvist, A.; Bent, S. F. A Brief Review of Atomic Layer Deposition: From Fundamentals to Applications. *Mater. Today* **2014**, *17* (5), 236–246. https://doi.org/10.1016/j.mattod.2014.04.026.

(33) Shekhah, O.; Wang, H.; Kowarik, S.; Schreiber, F.; Paulus, M.; Tolan, M.; Sternemann, C.; Evers, F.; Zacher, D.; Fischer, R. A.; Wöll, C. Step-by-Step Route for the Synthesis of Metal–Organic Frameworks. *J. Am. Chem. Soc.* **2007**, *129* (49), 15118–15119. https://doi.org/10.1021/ja076210u.

(34) Shekhah, O.; Eddaoudi, M. The Liquid Phase Epitaxy Method for the Construction of Oriented ZIF-8 Thin Films with Controlled Growth on Functionalized Surfaces. *Chem. Commun.* **2013**, *49* (86), 10079. https://doi.org/10.1039/c3cc45343j.

(35) Salmi, L. D.; Heikkilä, M. J.; Vehkamäki, M.; Puukilainen, E.; Ritala, M.; Sajavaara, T. Studies on Atomic Layer Deposition of IRMOF-8 Thin Films. *J. Vac. Sci. Technol. A* **2014**, *33* (1), 01A121. https://doi.org/10.1116/1.4901455.

(36) Salmi, L.; Heikkilä, M.; Puukilainen, E.; Sajavaara, T.; Grosso, D.; Ritala, M. Studies on Atomic Layer Deposition of MOF-5 Thin Films. *Microporous and Mesoporous Mater.* **2013**, *182*, 147–154. https://doi.org/10.1016/j.micromeso.2013.08.024.

(37) Ahvenniemi, E.; Karppinen, M. Atomic/Molecular Layer Deposition: A Direct Gas-Phase Route to Crystalline Metal–Organic Framework Thin Films. *Chem. Comm.* **2016**, 52 (6), 1139–1142. https://doi.org/10.1039/C5CC08538A.

(38) Lausund, K. B.; Nilsen, O. All-Gas-Phase Synthesis of UiO-66 through Modulated Atomic Layer Deposition. *Nat. Commun.* **2016**, *7* (1), 13578. https://doi.org/10.1038/ncomms13578.

(39) Lausund, K. B.; Petrovic, V.; Nilsen, O. All-Gas-Phase Synthesis of Amino-Functionalized UiO-66 Thin Films. *Dalton Trans.* **2017**, *46* (48), 16983–16992. https://doi.org/10.1039/C7DT03518G.

(40) Tanskanen, A.; Karppinen, M. Iron-Terephthalate Coordination Network Thin Films Through In-Situ Atomic/Molecular Layer Deposition. *Sci. Rep* **2018**, *8* (1), 8976. https://doi.org/10.1038/s41598-018-27124-7.

(41) Han, S.; Ciufo, R. A.; Meyerson, M. L.; Keitz, B. K.; Mullins, C. B. Solvent-Free Vacuum Growth of Oriented HKUST-1 Thin Films. *J. Mater. Chem. A* **2019**, *7* (33), 19396–19406. https://doi.org/10.1039/C9TA05179A.

(42) Multia, J.; Karppinen, M. Atomic/Molecular Layer Deposition for Designer's Functional Metal–Organic Materials. *Adv. Mater. Interfaces* **2022**, *9* (15), 2200210. https://doi.org/10.1002/admi.202200210.

(43) Han, S.; Ciufo, R. A.; Wygant, B. R.; Keitz, B. K.; Mullins, C. B. Methanol Oxidation Catalyzed by Copper Nanoclusters Incorporated in Vacuum-Deposited HKUST-1 Thin Films. *ACS Catal.* **2020**, *10* (9), 4997–5007. https://doi.org/10.1021/acscatal.0c00592.

(44) Multia, J.; Kravchenko, D. E.; Rubio-Giménez, V.; Philip, A.; Ameloot, R.; Karppinen, M. Nanoporous Metal–Organic Framework Thin Films Prepared Directly from Gaseous Precursors by Atomic and Molecular Layer Deposition: Implications for Microelectronics. *ACS Appl. Nano Mater.* **2023**, *6* (2), 827–831. https://doi.org/10.1021/acsanm.2c04934.

(45) Lausund, K. B.; Olsen, M. S.; Hansen, P.-A.; Valen, H.; Nilsen, O. MOF Thin Films with Bi-Aromatic Linkers Grown by Molecular Layer Deposition. *J. Mater. Chem. A* **2020**, *8* (5), 2539–2548. https://doi.org/10.1039/C9TA09303F.

(46) Ahvenniemi, E.; Karppinen, M. Atomic/Molecular Layer Deposition: A Direct Gas-Phase Route to Crystalline Metal–Organic Framework Thin Films. *Chem. Commun.* **2016**, *52* (6), 1139–1142. https://doi.org/10.1039/C5CC08538A.

(47) Medishetty, R.; Zhang, Z.; Sadlo, A.; Cwik, S.; Peeters, D.; Henke, S.; Mangayarkarasi, N.; Devi, A. Fabrication of Zinc-Dicarboxylate- and Zinc-Pyrazolate-Carboxylate-Framework Thin Films through Vapour–Solid Deposition. *Dalton Trans.* **2018**, *47* (40), 14179–14183. https://doi.org/10.1039/C8DT00352A.

(48) Khayyami, A.; Philip, A.; Karppinen, M. Atomic/Molecular Layer Deposited Iron–Azobenzene Framework Thin Films for Stimuli-Induced Gas Molecule Capture/Release. *Angew. Chem., Int. Ed.* **2019**, *58* (38), 13400–13404. https://doi.org/10.1002/anie.201908164.

(49) Silva, R. M.; Carlos, L. D.; Rocha, J.; Silva, R. F. Luminescent Thin Films of Eu-Bearing UiO-66 Metal Organic Framework Prepared by ALD/MLD. *Applied Surface Science* **2020**, 527, 146603. https://doi.org/10.1016/j.apsusc.2020.146603.

(50) Tao, J.; Wang, X.; Sun, T.; Cai, H.; Wang, Y.; Lin, T.; Fu, D.; Ting, L. L. Y.; Gu, Y.; Zhao, D. Hybrid Photonic Cavity with Metal-Organic Framework Coatings for the Ultra-Sensitive Detection of Volatile Organic Compounds with High Immunity to Humidity. *Sci. Rep.* **2017**, *7* (1), 41640. https://doi.org/10.1038/srep41640.

(51) Alfonso, F.; English, T. ALD Precursor Delivery & Debugging: A Case Study in Polymer Development. https://snfexfab.stanford.edu/docs/presentation/ald-precursor-delivery-debugging-case-study-in-polymer-development-final-presentation (accessed on 2022/04/05).

(52) Kräuter, M.; Cruz, A. J.; Stassin, T.; Rodríguez-Hermida, S.; Ameloot, R.; Resel, R.; Coclite, A. M. Influence of Precursor Density and Conversion Time on the Orientation of Vapor-Deposited ZIF-8. *Crystals* **2022**, *12* (2), 217. https://doi.org/10.3390/cryst12020217.

(53) Kwon, H. T.; Jeong, H.-K.; Lee, A. S.; An, H. S.; Lee, T.; Jang, E.; Lee, J. S.; Choi, J. Defect-Induced Ripening of Zeolitic-Imidazolate Framework ZIF-8 and Its Implication to Vapor-Phase Membrane Synthesis. *Chem. Commun.* **2016**, 52 (78), 11669–11672. https://doi.org/10.1039/C6CC05433A.

(54) Park, K. S.; Ni, Z.; Cote, A. P.; Choi, J. Y.; Huang, R.; Uribe-Romo, F. J.; Chae, H. K.; O'Keeffe, M.; Yaghi, O. M. CCDC 602542: Experimental Crystal Structure Determination. https://doi.org/10.5517/CCN6ZVN (accessed on 2021/12/21), 2006.

(55) Cliffe, M. J.; Mottillo, C.; Stein, R. S.; Bučar, D.-K.; Friščić, T. Accelerated Aging: A Low Energy, Solvent-Free Alternative to Solvothermal and Mechanochemical Synthesis of Metal–Organic Materials. *Chem. Sci.* **2012**, *3* (8), 2495–2500. https://doi.org/10.1039/C2SC20344H.

(56) Mottillo, C.; Lu, Y.; Pham, M.-H.; Cliffe, M. J.; Do, T.-O.; Friščić, T. Mineral Neogenesis as an Inspiration for Mild, Solvent-Free Synthesis of Bulk Microporous Metal-Organic Frameworks from Metal (Zn, Co) Oxides. *Green Chem.* **2013**, *15* (8), 2121–2131. https://doi.org/10.1039/C3GC40520F.

(57) Marreiros, J.; Dommelen, L. V.; Fleury, G.; Oliveira-Silva, R. de; Stassin, T.; Iacomi, P.; Furukawa, S.; Sakellariou, D.; Llewellyn, P. L.; Roeffaers, M.; Ameloot, R. Vapor-Phase Linker Exchange of the Metal–Organic Framework ZIF-8: A Solvent-Free Approach to Post-Synthetic Modification. *Angew. Chem., Int. Ed.* **2019**, *58* (51), 18471–18475. https://doi.org/10.1002/anie.201912088.

(58) Huang, J.-K.; Saito, N.; Cai, Y.; Wan, Y.; Cheng, C.-C.; Li, M.; Shi, J.; Tamada, K.; Tung, V. C.; Li, S.; Li, L.-J. Steam-Assisted Chemical Vapor Deposition of Zeolitic Imidazolate Framework. *ACS Materials Lett.* **2020**, 485–491. https://doi.org/10.1021/acsmaterialslett.0c00026.

(59) Shi, Q.; Chen, Z.; Song, Z.; Li, J.; Dong, J. Synthesis of ZIF-8 and ZIF-67 by Steam-Assisted Conversion and an Investigation of Their Tribological Behaviors. *Angew. Chem., Int. Ed.* **2011**, 50 (3), 672–675. https://doi.org/10.1002/anie.201004937.

(60) Herold, R. J.; Aggarwal, S. L.; Neff, V. MECHANISMS OF THE REACTIONS OF DIETHYLZINC WITH ISOPROPANOL AND WATER. *Can. J. Chem.* **1963**, *41* (5), 1368–1380. https://doi.org/10.1139/v63-187.

(61) Regoutz, A.; Mascheck, M.; Wiell, T.; Eriksson, S. K.; Liljenberg, C.; Tetzner, K.; Williamson, B. A. D.; Scanlon, D. O.; Palmgren, P. A Novel Laboratory-Based Hard X-Ray Photoelectron Spectroscopy System. *Rev. Sci. Instrum.* **2018**, *89* (7), 073105. https://doi.org/10.1063/1.5039829.

(62) Liu, C.; Wang, J.; Wan, J.; Yu, C. MOF-on-MOF Hybrids: Synthesis and Applications. *Coord. Chem. Rev.* **2021**, *432*, 213743. https://doi.org/10.1016/j.ccr.2020.213743.

(63) Avci, C.; Liu, Y.; Pariente, J. A.; Blanco, A.; Lopez, C.; Imaz, I.; Maspoch, D. Template-Free, Surfactant-Mediated Orientation of Self-Assembled Supercrystals of Metal–Organic Framework Particles. *Small* **2019**, *15* (31), 1902520. https://doi.org/10.1002/smll.201902520.

Table of Contents

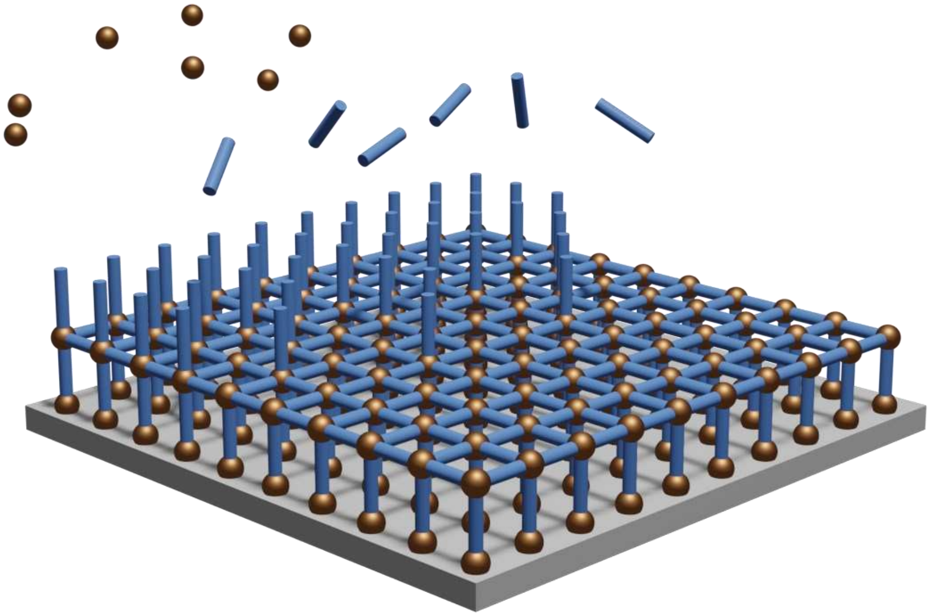

Supporting Information

Molecular layer deposition of zeolitic imidazolate framework-8 films

---

Jorid Smets,[a,b,‡] Alexander John Cruz,[a,c,d,‡,†] Víctor Rubio-Giménez,[a] Max L. Tietze,[a] Dmitry E. Kravchenko,[a] Giel Arnauts,[a] Aleksander Matavž,[a] Nathalie Wauteraerts,[a] Min Tu,[a,§] Kristof Marcoen,[c] Inhar Imaz,[e] Daniel Maspoch,[e,g] Maxim Korytov,[d] Philippe M. Vereecken,[a,d] Steven De Feyter,[f] Tom Hauffman,[c] and Rob Ameloot[a,*]

---

[a] Center for Membrane Separations, Adsorption, Catalysis, and Spectroscopy (cMACS), KU Leuven - University of Leuven, Celestijnenlaan 200F, Leuven, 3001, Belgium

[b] Sustainable Energy, Air & Water Technology (DuEL), Department of Bioscience Engineering, University of Antwerp, Groenenborgerlaan 171, 2020 Antwerp, Belgium

[c] Research Group of Electrochemical and Surface Engineering, Department of Materials and Chemistry, Vrije Universiteit Brussel, Pleinlaan 2, Brussels, 1050, Belgium

[d] Imec, Kapeldreef 75, Leuven, 3001, Belgium

[e] Catalan Institute of Nanoscience and Nanotechnology (ICN2), CSIC and The Barcelona Institute of Science and Technology, Campus UAB, Bellaterra, 08193 Barcelona, Spain

[f] Department of Chemistry, Division of Molecular Imaging and Photonics, KU Leuven, Leuven, Belgium

[g] ICREA Pg. LluísCompanys 23, 08010 Barcelona, Spain

‡ These authors contributed equally.

† Baker Hughes, Schumanplein 6, Brussels 1040 Belgium

§ 2020 X-Lab and State Key Laboratory of Transducer Technology, Shanghai Institute of Microsystem and Information Technology, Chinese Academy of Sciences, Shanghai 200050, China

E-mail: rob.ameloot@kuleuven.be

Table of Contents

Supporting Information

Methods

Substrates: Device grade, p-type, 200 mm Si wafers (Si-Mat, resistivity = 1-30 Ω cm, thickness = 725 ± 25 μm) were used and smaller pieces were cleaved.

Solution-deposited films: ZIF-8 thin films were synthesized using a previously described deposition route by Lu and Hupp.[1] In short, a silicon substrate was first cleaned in piranha solution and extensively washed with deionized water and methanol. Then, the substrate was immersed in the mixture of 2-methylimidazole (50 mM; Sigma Aldrich, 99%) and zinc nitrate hexahydrate (25 mM; Alfa Aesar, 99%) solutions for 30 min. The deposition step was repeated several times to adjust the final film thickness. After the last layer deposition, the sample was washed 3 times in methanol and once in ethanol, and dried under nitrogen flow.

ZIF-8 MOF-CVD: Chemical vapor deposition of ZIF-8 was performed in the same ALD reactor used for ZIF-8 MLD (Savannah S-200 thermal ALD reactor, Veeco Instruments Inc.). The used process was according to our previous work.[2] The ZIF-8 CVD process employs deionized water (DIW), diethylzinc (DEZ, 97%, STREM), and freshly-ground HmIM (30 g, 99%, Sigma Aldrich) as precursors. Nitrogen (99.999%) was the carrier and purging gas used and sourced from a cleanroom header. First, 3 nm of zinc oxide is deposited by supplying alternating pulses (0.015 s) of DEZ and water, separated by N_2 purges (5 s). Afterward, the HmIM bubbler is heated and purged as described in the ZIF-8 MOF-MLD section. HmIM is bubbled to the reactor chamber in stopped-flow conditions until the ellipsometry profile of the monitoring substrate (Si wafer) is constant.

Ellipsometry during deposition: The optical properties of the deposited layers were measured during deposition using an M-2000x spectroscopic ellipsometer (J. A. Woollam Co. Inc., λ = 246-1000 nm), using a lid with fused silica viewports. The optical parameters of the layer were fit with an extended Cauchy model at the end of the deposition, these parameters are fixed while the thickness is calculated as a function of deposition time.

Cauchy equation: $n(\lambda) = A + \frac{B}{\lambda^2} + \frac{C}{\lambda^4}$

Urbach equation: $k(\lambda) = A_k e^{B_k(E-E_b)}$ if $k \neq 0$

Full-wafer thickness mapping: The thickness and refractive index (λ = 633 nm) of the ZIF-8 layers deposited on 200 mm wafers were measured with a KLA-Tencor ASET F5x thin film measurement system equipped with a motorized stage. A radial map of Psi and Delta (λ = 400-800 nm) was recorded for 100 points evenly distributed over the wafer.

Ellipsometric porosimetry: Known concentrations of methanol vapor in N_2 flow (420 s, 550 sccm) were generated by a home-built vapor dosing system and were alternated by N_2 purges (180 s, 550 sccm). The uptake of a film can be approximated by:[3]

$$\tau = \frac{l^2}{3D}$$

With τ the time constant, l the thickness of the MOF layer, and D the transport diffusion coefficient (from Chmelik *et al.*[4], 1e-12 m^2/s). The time constant for methanol diffusion in a 30 nm MOF film therefore is 3e-4 s. At 3τ, 95% of the pores will be filled, *i.e.*, after 9e-4 s. Thus the methanol exposure and purge times are sufficiently long to overcome diffusion limitations. The dosing experiment is plotted in **Figure S22** as a function of time and the points at which data for the isotherm graphs are exported are indicated in red.

The sample (30 cycles of ZIF-8 MLD) was situated in an environmental cell with fused silica viewports. The optical constants of the material were determined by ellipsometry with a Woollam iSE ellipsometer. For direct ZIF-8 MLD, the layer was modeled as an extended Cauchy layer. Afterward, all optical parameters and thickness were fixed except for A and B, these two values were fitted as a function of methanol vapor concentration, from which the refractive index at each point can be calculated. For two-step ZIF-8 MLD an effective medium approximation (Bruggemann) model was used to account for the partial surface coverage, combining a Cauchy model with a fitted void fraction (often about 10 vol%).[5]

$$f_{MOF}\frac{\tilde{\varepsilon}_{MOF}-\tilde{\varepsilon}_{EMA}}{\tilde{\varepsilon}_{MOF}+\ 2\tilde{\varepsilon}_{EMA}}+f_{void}\frac{\tilde{\varepsilon}_{void}-\tilde{\varepsilon}_{EMA}}{\tilde{\varepsilon}_{void}+\ 2\tilde{\varepsilon}_{EMA}}=0$$

With $\tilde{\varepsilon}$ the effective complex dielectric function, and f the volume fraction of each constituent.

When the void fraction is not included in the modelling, a lower refractive index is modeled (n = 1.21).

Atomic Force Microscopy (AFM): Topography images were recorded in intermittent contact mode using an NX-Hivac (Park Systems) under Ar atmosphere, an Agilent AFM 5100, and a Bruker multimode 8 setup under ambient conditions using Pt/Ir cantilevers for the first system and Si cantilevers (AC160TS-R3, Olympus Corporation) for the two other ones. Data analysis was performed using WSXM 5.0 software.[6]

Grazing incidence and specular X-ray diffraction (GIXRD and sXRD): Diffraction patterns were recorded using a Malvern PANalytical Empyrean diffractometer equipped with a Cu anode operating at 45 kV and 40 mA and PIXcel3D solid-state detector. Thin film samples were placed on a flat stage and measured in scanning line mode with a step size of 0.053° and a counting time of 1000 s per step. On the incident beam side, a 1/32° fixed anti-scatter slit was used to limit the divergence of the beam. Additionally, a 1/8° divergence slit and a 4 mm beam mask were used. At the secondary side, a 1/8° anti-scatter slit together with a 0.04 Soller slit were used. For GIXRD measurements an incident beam angle of 0.2° was used.

Synchrotron GIXRD: Measurements were carried out at the BL9 beamline of DELTA synchrotron (λ = 1.03 Å; Dortmund, Germany)[7] and the XRD1 beamline of the Elettra Synchrotron (λ = 1.4 Å; Trieste, Italy) using a stationary MAR or Pilatus 2M detector, respectively. Thin film samples were placed on sample holders mounted on multi-axis diffractometers at distances of approximately 350 and 200 mm, respectively (both calibrated with LaB_6 reference samples). Multiple pixel images were acquired at various angles of incidence and then further processed into diffractograms and reciprocal space maps using FIT2D[8] and GIDVis[9] software packages. All integrated diffractograms were converted from Q to 2θ using CuKα wavelength 1.54 Å.

Hard X-ray photoelectron spectroscopy (HAXPES): Hard X-ray photoemission spectroscopy measurements were performed at IMO-IMOMEC (Hasselt University, Belgium) with a HAXPES lab system (Scienta Omicron, Sweden, Germany) equipped with a liquid gallium jet source (Excillum MetalJet D2; Excillum, Sweden) and a monochromator (HAX9-5; Scienta Omicron) for generating a monochromized (420 meV) Ga Kα beam of hν = 9251.6 eV. A 200 mm hemispherical analyzer (R4000, Scienta Omicron) combined with a 40 mm microchannel plate/charge-coupled device detector (MCP/CCD, VG Scienta) with 435 channels was used for photoelectron detection. A slit of 1.0 mm and pass energies of 500 and 200 eV were used for survey and core-level scans, respectively. For the latter, this configuration yields an energy resolution of 660 meV. To verify the correct energy calibration of the instrument under Ga Kα, Au 4f core level scans on a gold reference foil were performed. The hard X-ray beam exiting the monochromator and the analyzer is aligned under a right angle while the sample is tilted by ca. 3° w.r.t. to the incident X-ray beam. Before the measurements, the samples were stored in nitrogen. To estimate atomic ratios, recently published theoretical elemental photoemission cross sections for Ga Kα excitation were used, as in our previous work on ZIF-8 CVD films.[10,11]

Conductive (c-)AFM: A Bruker's Dimension Icon AFM system was used to check for pinholes in films on Si substrates. The samples were electrically contacted with Ag paint using a custom sample holder. A heavily doped full diamond tip was used to test the samples with an applied DC bias voltage of 8.0 V at a scan speed of 0.5 Hz. The threshold bias voltage for the direct ZIF-8 MLD coating was determined to be > 5.0 V. All c-AFM measurements were carried out in a glove box under an Ar atmosphere.

Synthesis and formation of ZIF-8 and ZIF-67 supercrystals: $Zn(OAc)_2{\cdot}2H_2O$ (99%) [for ZIF-8] and $Co(Ac)_2.4H_2O$ (99%) [for ZIF-67] in DI water were separately added into HmIM (95%) and cetyltrimethylammonium bromide (99%) solutions. The mixture was stirred and left for 2 h to form the ZIF crystals. After washing, the crystals were suspended in water and dropcasted on Si substrates. The coated substrates were dried and activated in an oven at 120 °C.[12]

Electron microscopy: Scanning electron microscopy (SEM) images were collected using a Philips XL30 FEG and a JEOL JSM 6010-LV. Before imaging, the samples were coated with 3-5 nm of Pt.

Infrared spectroscopy (IR): A Varian 670 Fourier Transform-IR spectrometer with an actively cooled mercury cadmium telluride detector and a Ge crystal plate in the Veemax III module was used for all measurements. For films on Si, the system was used in attenuated total internal reflection configuration; for powders, a Varian 620 FTIR imaging microscope with a slide-on Ge ATR tip was employed.

Thermogravimetric Analysis (TGA): TGA for vapor pressure determination of the HmIM linker was carried out in a Netzsch STA 449 F3 Jupiter TG analyzer under vacuum ($2{\times}10^{-2}$ mbar). The sample was placed in a Knudsen cell with a 122 µm orifice in the lid. The vapor pressure was calculated from the mass loss rate at the isothermal segments according to the Knudsen cell effusion equation.[13] The calculations for the estimation of the vapor pressure curves are detailed below. The same apparatus was used for the characterization of the ZIF-67 crystals.

Table S1 | Summary of some of the reported vapor-phase processes for the layer-by-layer deposition of MOFs and non-porous coordination polymers.

References	Material	Precursors		Activation protocol/ treatments*	Dep. temp. [°C]	Film thickness monitoring	GPC [nm]	Porosity assessment
Salmi, *et al.*[14]	MOF-5	ZnAc$_2$	1,4-BDC	RH (60%) 24 h DMF, 150 °C, 2 h autoclave	225, 350	*ex situ*: reflectance (optical)	0.65	IPA uptake: micro- and mesoporosity
Salmi, *et al.*[15]	IRMOF-8	ZnAc$_2$	2,6-NDC	RH (70%) 24 h DMF, 150 °C, 2 h autoclave	260, 300	*ex situ*: reflectance SEM-EDS	0.49	Pd loading and EDS mapping
Ahvenniemi and Karppinen[16]	Cu-terephtalate	Cu(thd)$_2$	TPA	n/a	180, 280	*ex situ*: XRR	0.75	H_2O uptake
Multia, *et al.*[17]	Cu-terephtalate	Cu(thd)$_2$	TPA	2 h @150°C for Kr ads., @40°C for MeOH ads.	180, 220	*ex situ*: XRR	0.22	Kr, MeOH uptake
Medishetty, Devi, *et al.*[18]	Zn-di -carboxylate- Zn-pyrazolate-carboxylate	(DMA)$_2$ [Zn$_3$(BDC)$_4$] Zn$_4$O (dmcapz)$_6$	TPA	closed-cell heat treatment at 120 °C, 24 h	170, 240, 120	*ex situ*: ellipsometry and SEM	n/a	n/a
Ahvenniemi and Karppinen[19]	Ca-TPA	Ca(thd)$_2$	TPA	n/a	190, 420	*ex situ*: XRR	0.34	n/a
Lausund and Nilsen[20]	UiO-66	ZrCl$_4$	1,4-BDC	acetic acid modulation, 160 °C autoclave	235, 390	*in situ*: QCM	0.7	QCM H_2O uptake (~1.9 wt %)
Lausund, Nilsen, *et al.*[21]	amino func. UiO-66	ZrCl$_4$	2-amino -1,4 BDC	acetic acid modulation, 160 °C autoclave	240, 390	*in situ*: QCM	1	QCM H_2O uptake
Lausund, Nilsen, *et al.*[22]	UiO-66 with bi-aromatic linkers	ZrCl$_4$	NDC BPDC	acetic acid modulation, 160 °C autoclave	260, 390	*in situ*: QCM	0.5-1.5	QCM H_2O uptake
Tanskanen and Karppinen[23]	Fe-terephthalate	FeCl$_3$	TPA	n/a	240, 260	*ex situ*: XRR	1.1	n/a
Han *et al.*[24]	HKUST-1	Cu	BTC	annealing under H_2O and O_2 exposure	50	*ex situ*: AFM	n/a	H_2O uptake
Khayyami *et al.*[25]	Fe-azobenzene	FeCl$_3$	azo BDC	n/a	250, 290	*ex situ*: XRR	2.5	H_2O uptake
Silva *et al.*[26]	Eu-bearing UiO-66	Eu(thd)$_3$	NH$_2$TA	n/a	180	*ex situ*: SEM	1.4	n/a

MOF-5 = $Zn_4O(BDC)_3$; **ZnAc$_2$** = Zn acetate; **BDC** = benzene-1,4-dicarboxylate; **IPA** = isopropyl alcohol; **IRMOF-8** = $[Zn_4O(NDC)]_3$; **RH** = relative humidity; **NDC** = naphthalene-2,6-dicarboxylate; **BPDC** = biphenyl-4,40-dicarboxylic acid; **TP(A)** = terephthalic (acid); **thd** = 2,2,6,6-tetramethyl-3,5-heptanedione; **DMA** = dimethylammonium; **DMF** = dimethylformamide; **dmcapz** = 3,5-dimethyl-4-carboxypyrazole; **UiO-66** = $[Zr_6O_4(OH)_4][BDC]_6$; **HKUST-1** = $[Cu_3(OH_2)_3(BTC)_2]$, **BTC** = benzene-1,3,5-tricarboxylic acid; **Eu(thd)$_3$** = europium(III)-tris-(2,2,6,6-tetramethyl-3,5-heptanedionate); **NH$_2$TA** = 2-aminoterephthalic acid; **H.P.** = high pressure; **Dep. Temp.** = deposition temperature; **GPC** = growth per cycle; **XRR** = X-ray reflectivity; **AFM** = atomic force microscopy; **QCM** = quartz crystal microbalance; **SEM** = scanning electron microscopy; **EDS** = energy-dispersive X-ray spectroscopy. | ***post treatments of non-crystalline, as-deposited layers.

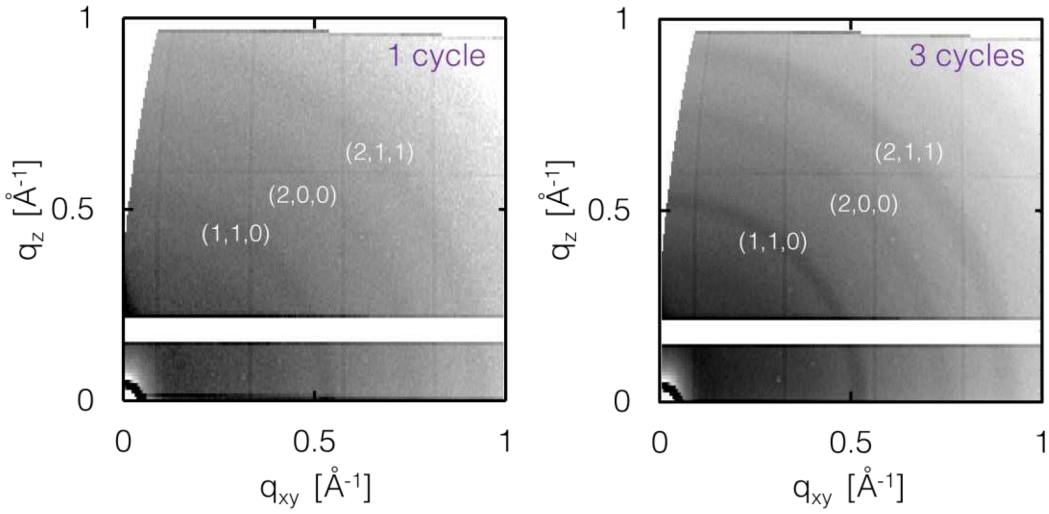

Figure S1 | Synchrotron GIXRD reciprocal space maps of direct ZIF-8 MLD showing crystallinity even at a very low number of cycles.

Vapor pressure determination of 2-methylimidazole (HmIM) *via* thermogravimetry: Knudsen effusion method

Using the Knudsen effusion method, the vapor pressure of HmIM was experimentally determined. With this method, the vapor pressure of the MOF-MLD linker is correlated to the weight loss at several temperature steps. The data collected is modeled with an empirical equation for the steady-state effusion of dilute gases.[27,28] This protocol has been previously demonstrated in various ALD precursors.[29]

The measurements were carried out under dynamic vacuum conditions using an inert process gas. The rate of mass loss ($\frac{dm}{dt}$) at a particular temperature was calculated (**Eqn. 1**) for a particular operating range and fed into the Knudsen equation.[30] The series of vapor measurements can then be fitted using the reduced Clausius-Clapeyron-derived equation (**Eqn. 2**), assuming that the ideal gas law is valid and the latent heat of vaporization is independent of the temperature.

$P_{sat} = \frac{dm}{dt}\frac{\sqrt{\frac{2\pi RT}{M}}}{AK_c}$	[Pa]	vapor pressure at temperature, T [K]	***Eqn.* 1**
$A = \pi r^2$	[m^2]	area of the Knudsen cell orifice	
M	[g mol^{-1}]	molecular weight of the linker	
$\frac{dm}{dt}$	[kg s^{-1}]	rate of change of mass at temperature, T [K]	
$K_c = \frac{1}{1+\frac{3l}{8r}}$		Clausing coefficient[a),b)]	

$l = 0.0003$ [m] length of the Knudsen cell orifice

$r = 4.86 \times 10^6$ [m] radius of the Knudsen cell orifice

[a] a simplified multiplying factor to take into account the resistance of the membrane (orifice) to effusion due to its definite thickness.

[b] this simplification of the Clausing coefficient is valid for experimental conditions where the Knudsen number (ratio of the mean free path to the orifice diameter) is ≥ 10, which is applicable in our process implemented in this work.[31]

$$\ln P = A + \frac{B}{T[K]} \qquad \textbf{\textit{Eqn. 2}}$$

The data is found to be in agreement with the reported values (**Figure S2**).[32,33]

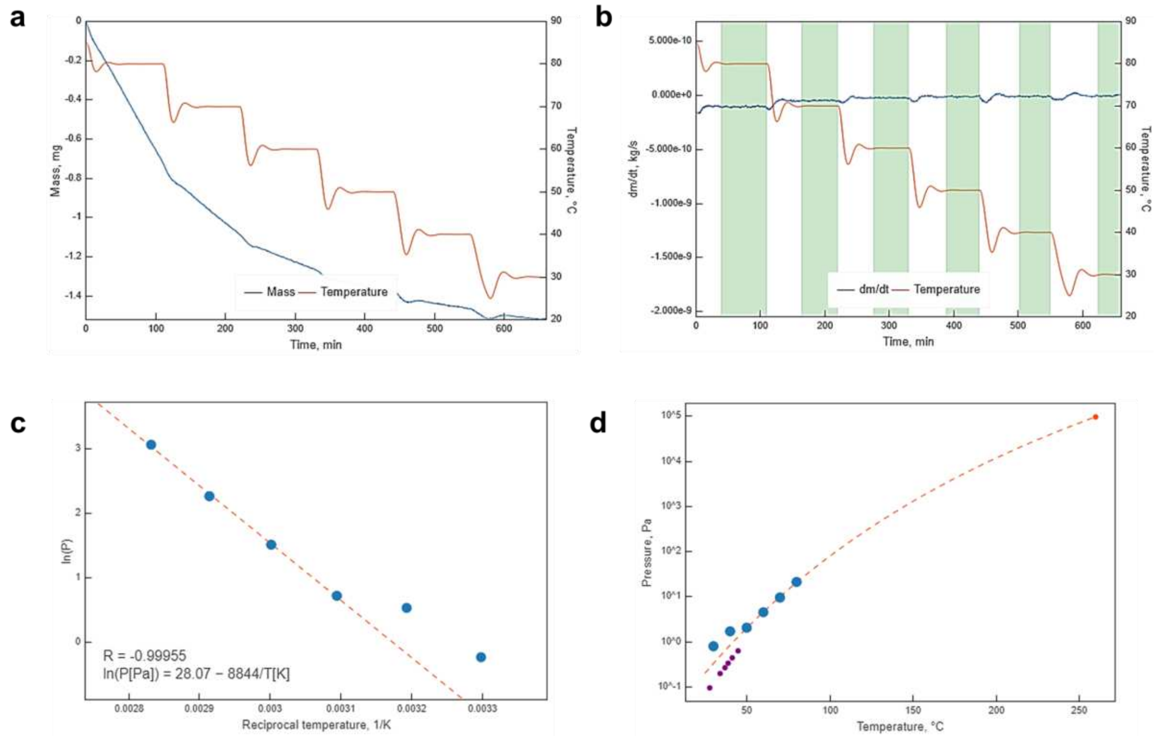

Figure S2 | Vapor pressure determination of 2-methylimidazole. a) Mass loss at different temperature steps as a function of time. **b)** Mass loss derivative at different temperatures as a function of time. The green vertical segments indicate the isothermal steps. **c)** Calculated values with the derived Clausius-Clapeyron plot, and **d)** calculated vapor pressure at the operating temperature range of interest. Experimental data from literature[32] are added (purple dots) showing good agreement with the values obtained in this work.

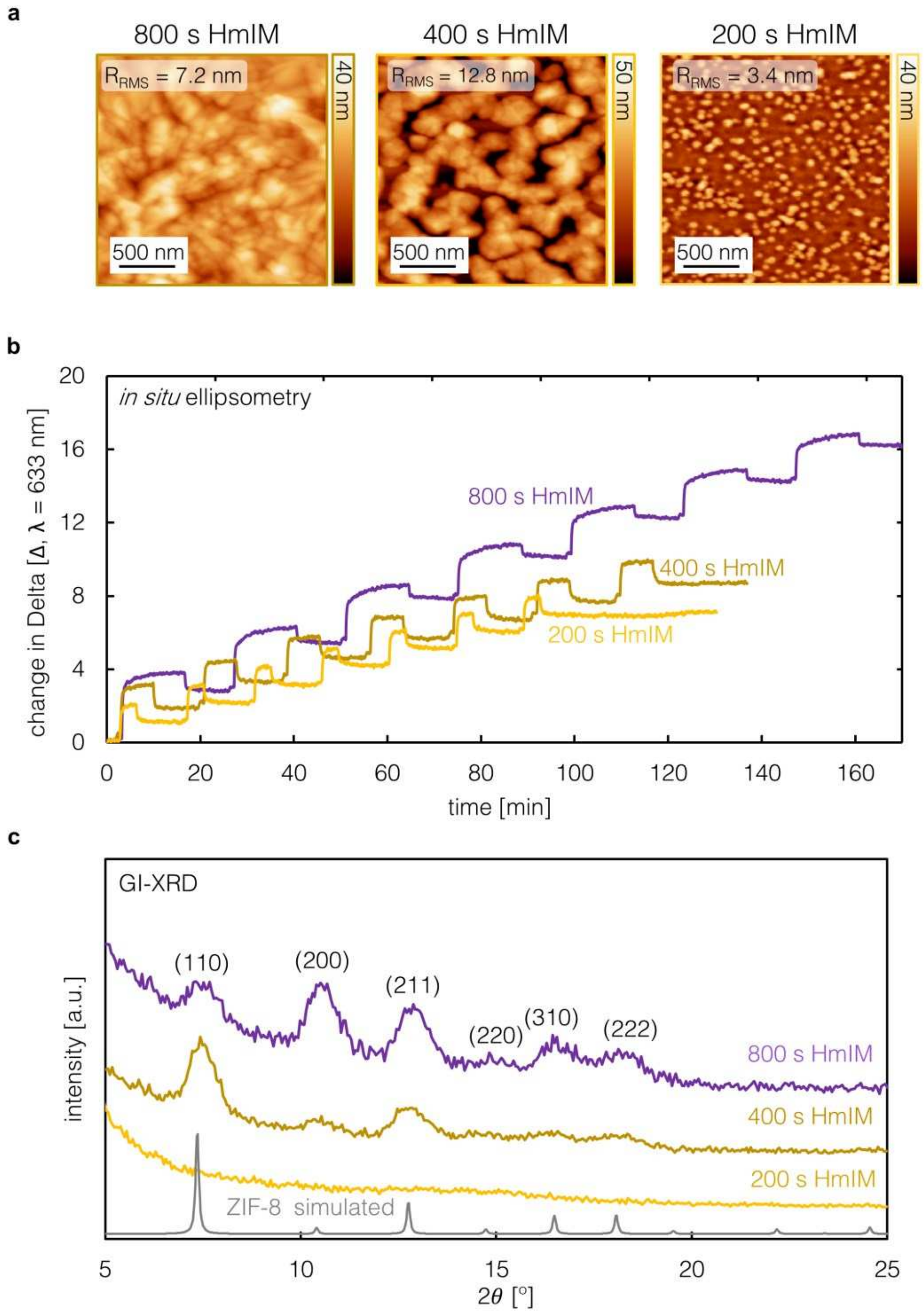

Figure S3 | Direct ZIF-8 MLD linker exposure times. a) AFM images of the MOF-MLD ZIF-8 layer (30 cycles) using different linker (HmIM) exposure times: 800 s (full exposure, purple), 400 s (50% of full exposure, brown), and 200 s (25% of full exposure, yellow) with all other process parameters held constant. **b)** Corresponding *in situ* ellipsometry profiles (change in the ellipsometric parameter, Delta, λ = 633 nm), and **c)** GIXRD of the as-deposited films (including an activated sample for the 50% t_{HmIM} sample). The AFM roughness (R_{RMS}) values are calculated for a 2 × 2 μm^2 probe area.

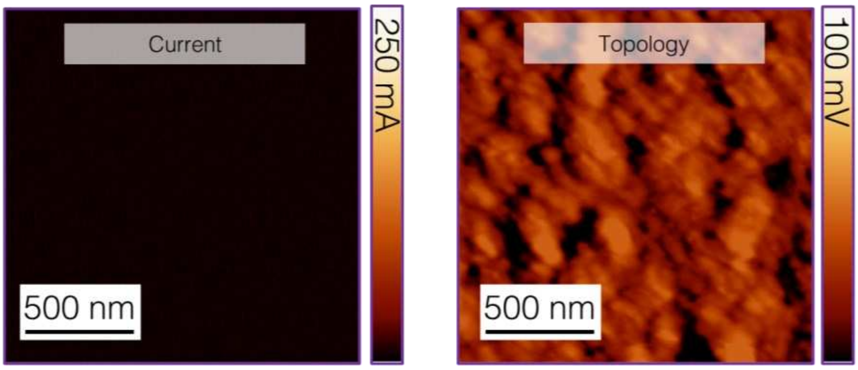

Figure S4 | Direct ZIF-8 MLD films on Si are pinhole-free. Conductive AFM of 10 cycles of direct ZIF-8 MLD.

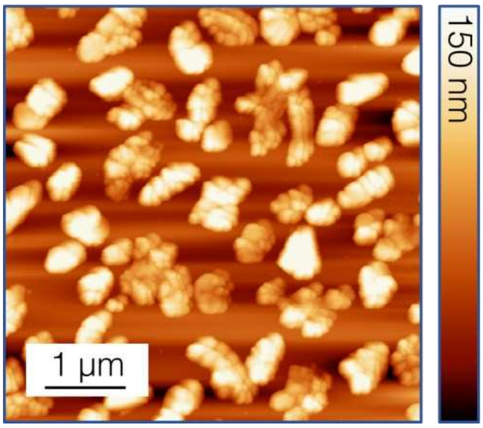

Figure S5 | AFM image of a MOF-CVD ZIF-8 "layer", i.e., scattered crystallites, using 1.8 nm ALD ZnO as the precursor.

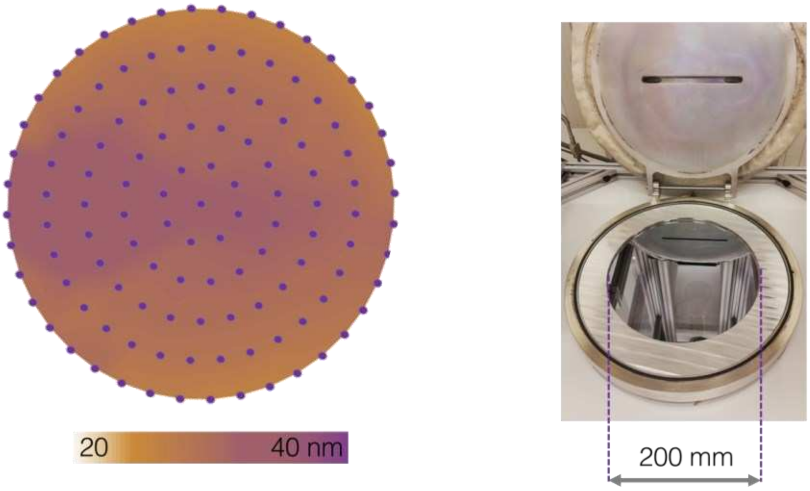

Figure S6 | Photograph of a 200 mm wafer with 30 MLD ZIF-8 cycles and the corresponding 100-point ellipsometry thickness mapping.

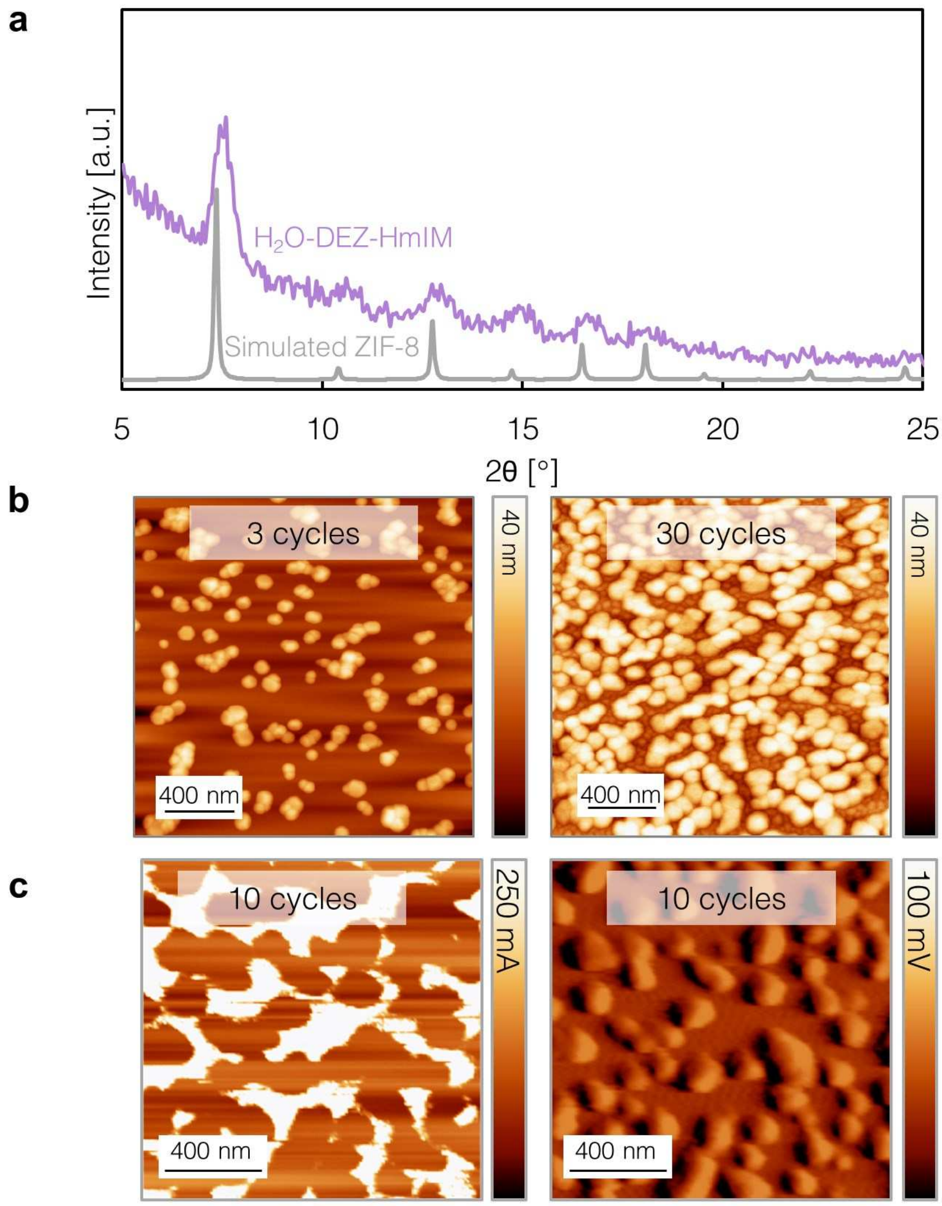

Figure S7 | Film characterization of direct ZIF-8 MLD with a missing water pulse. H_2O-DEZ-HmIM instead of H_2O-DEZ-H_2O-HmIM **a)** GIXRD shows crystalline features, with only the (110) at 7.3° strongly visible. **b)** AFM shows a tendency towards island growth. **c)** c-AFM shows pinholes at 10 cycles of MOF-MLD.

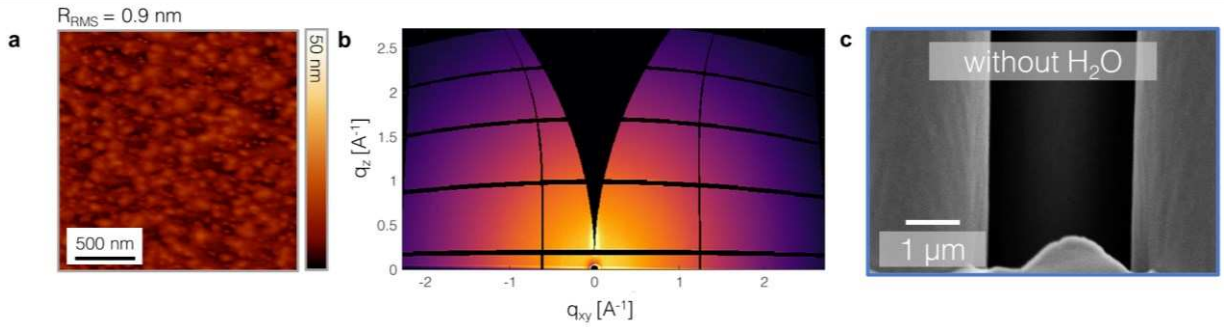

Figure S8 | Effect of no water pulses in direct ZIF-8 MLD. a) AFM image, **b)** synchrotron GIXRD reciprocal space map, and **c)** SEM image of deposition on high-aspect-ratio pillar of direct ZIF-8 MLD without any water included.

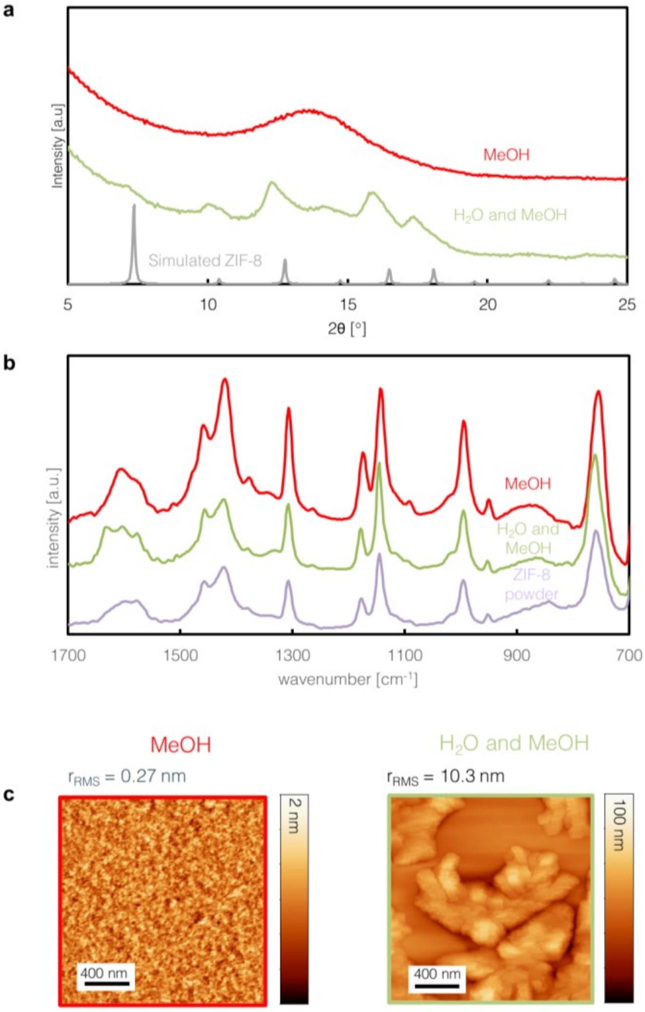

Figure S9 | Direct ZIF-8 MLD (30 cycles) with water entirely or partially substituted by methanol. a) GIXRD pattern, **b)** ATR-FTIR spectra, and **c)** AFM images comparing complete substitution of water with methanol (red), partial substitution (green), and a reference powder (purple).

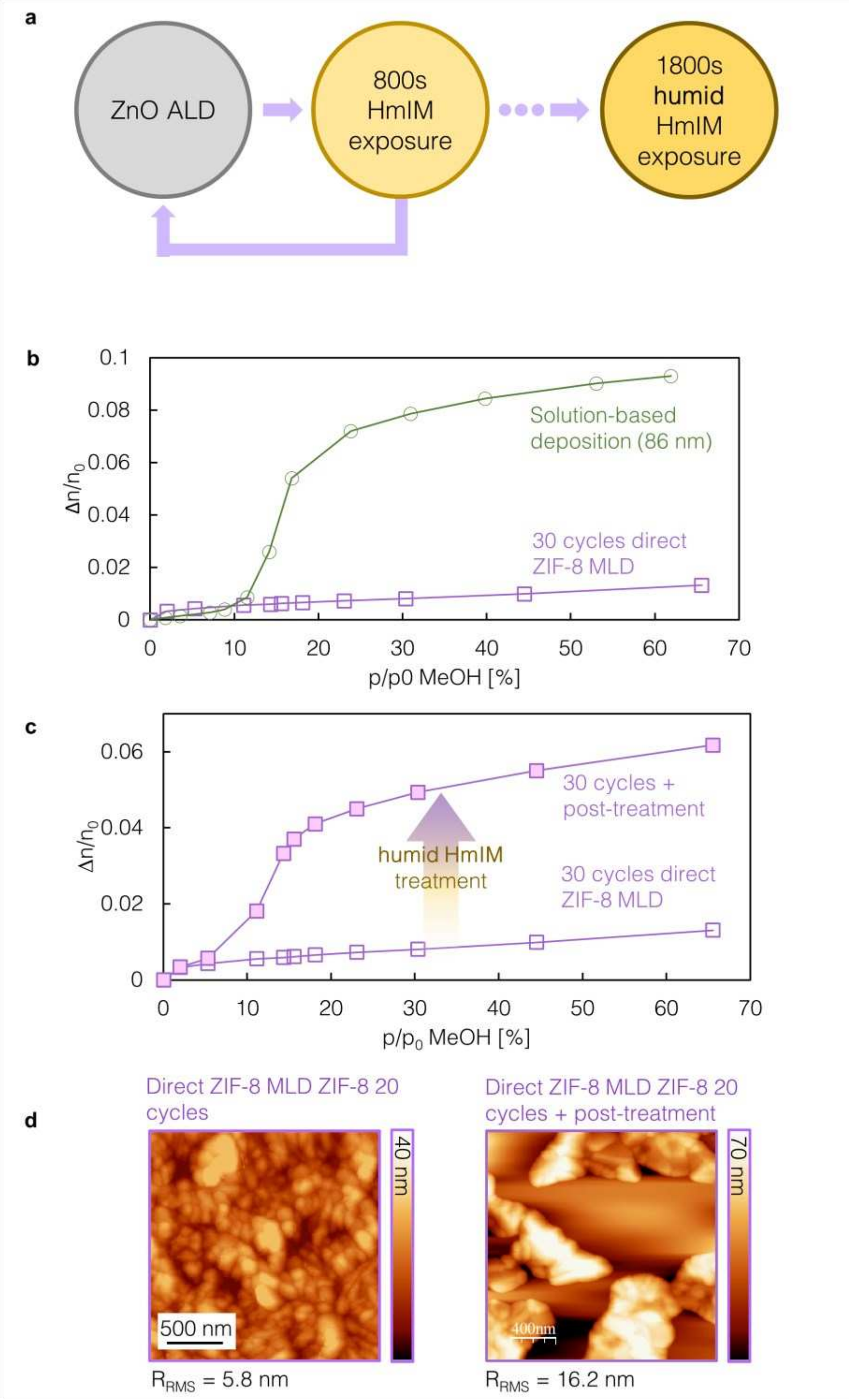

Figure S10 | Humidified conditions HmIM post-deposition treatment of direct ZIF-8 MLD. a) Schematic of direct ZIF-8 MLD followed by humidified conditions post-deposition treatment. **b)** Ellipsometric porosimetry comparing direct ZIF-8 MLD and solution deposited ZIF-8 (deposited according to Lu and Hupp[1]). **c)** Ellipsometric porosimetry, comparison with as-deposited direct ZIF-8 MLD, and humidified conditions HmIM post-treated sample. Both films are modelled with an extended Cauchy model. **d)** Comparison in morphology and coverage of an as-deposited and a post-deposition treated sample.

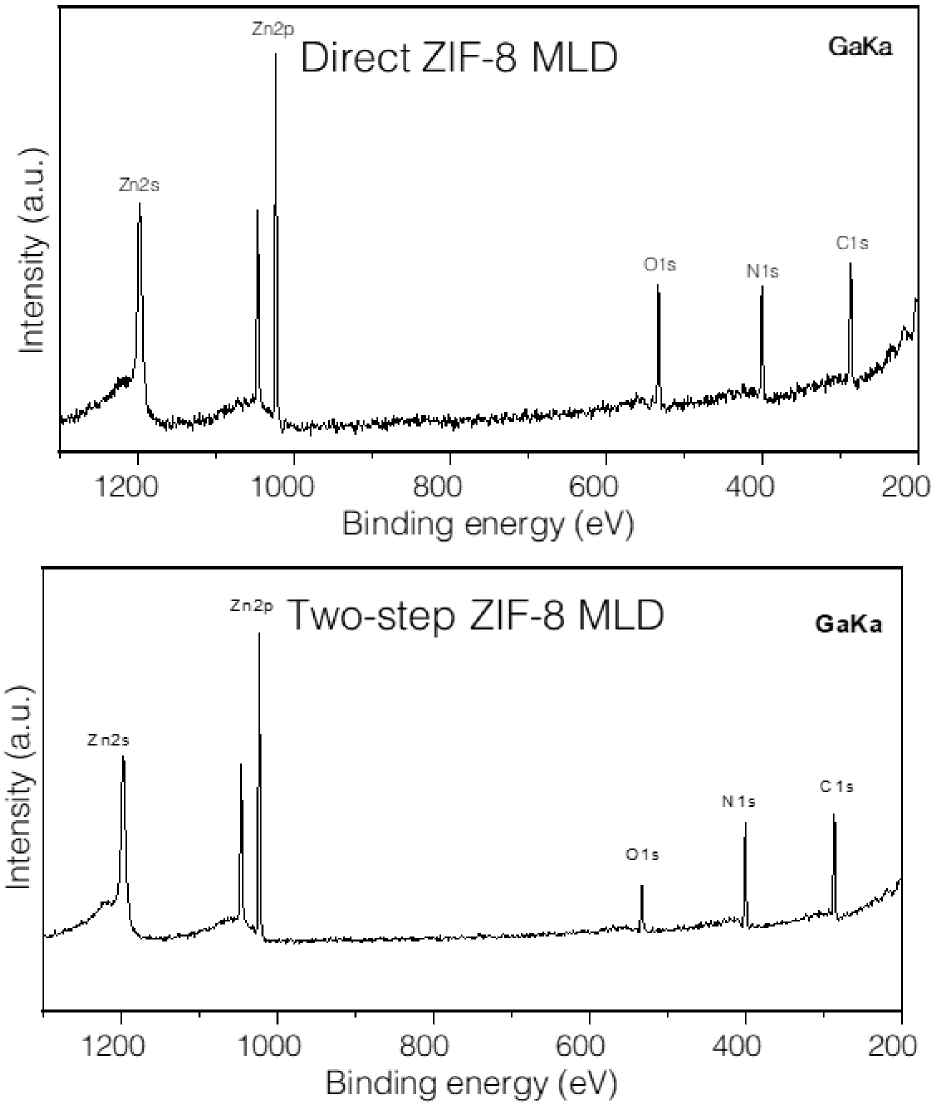

Figure S11 | Hard X-ray photoelectron spectroscopy (HAXPES) survey scans for direct ZIF-8 MLD (top, 10 cycles, ~10 nm) and two-step ZIF-8 MLD (bottom, ~27 nm). Exposure to air was minimized by packaging the samples in nitrogen immediately after deposition for transport to the spectrometer. For direct ZIF-8 MLD an increased oxygen signal is visible. This observation can be attributed to the SiO_2 signal from the native oxide, which is less present for two-step ZIF-8 MLD due to the increased thickness. Furthermore, the increased presence of oxygen can partially be attributed to a higher defect concentration.

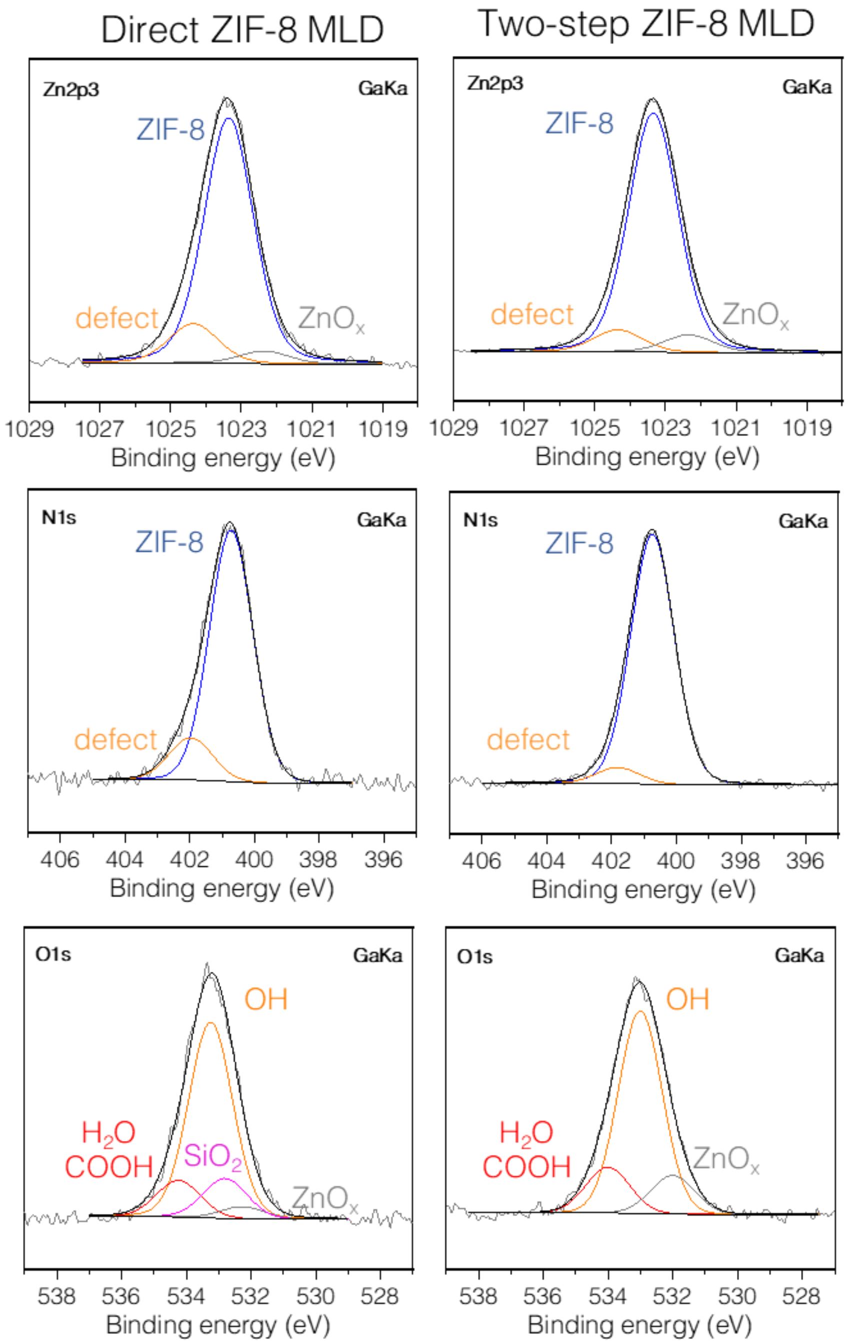

Figure S12 | HAXPES peak fitting for direct ZIF-8 MLD (left, 10 cycles, ~10 nm) and two-step ZIF-8 MLD (right, 30 cycles, ~27 nm). Exposure to air was minimized by packaging the samples in nitrogen immediately after deposition for transport to the spectrometer. For the zinc and nitrogen peaks, subpeaks characteristic of ZIF-8 are shown in blue, and in orange high energy defects peaks are plotted, which cannot be identified since various potential defect peaks are overlapping. A lower intensity of this defect peak is fitted for two-step ZIF-8 MLD. Therefore, these films approach the ideal ZIF-8 structure more closely. In the oxygen peak OH (orange), H_2O or carboxyl (red), ZnOx (grey), and SiO_2 (pink) subpeaks can be fitted.

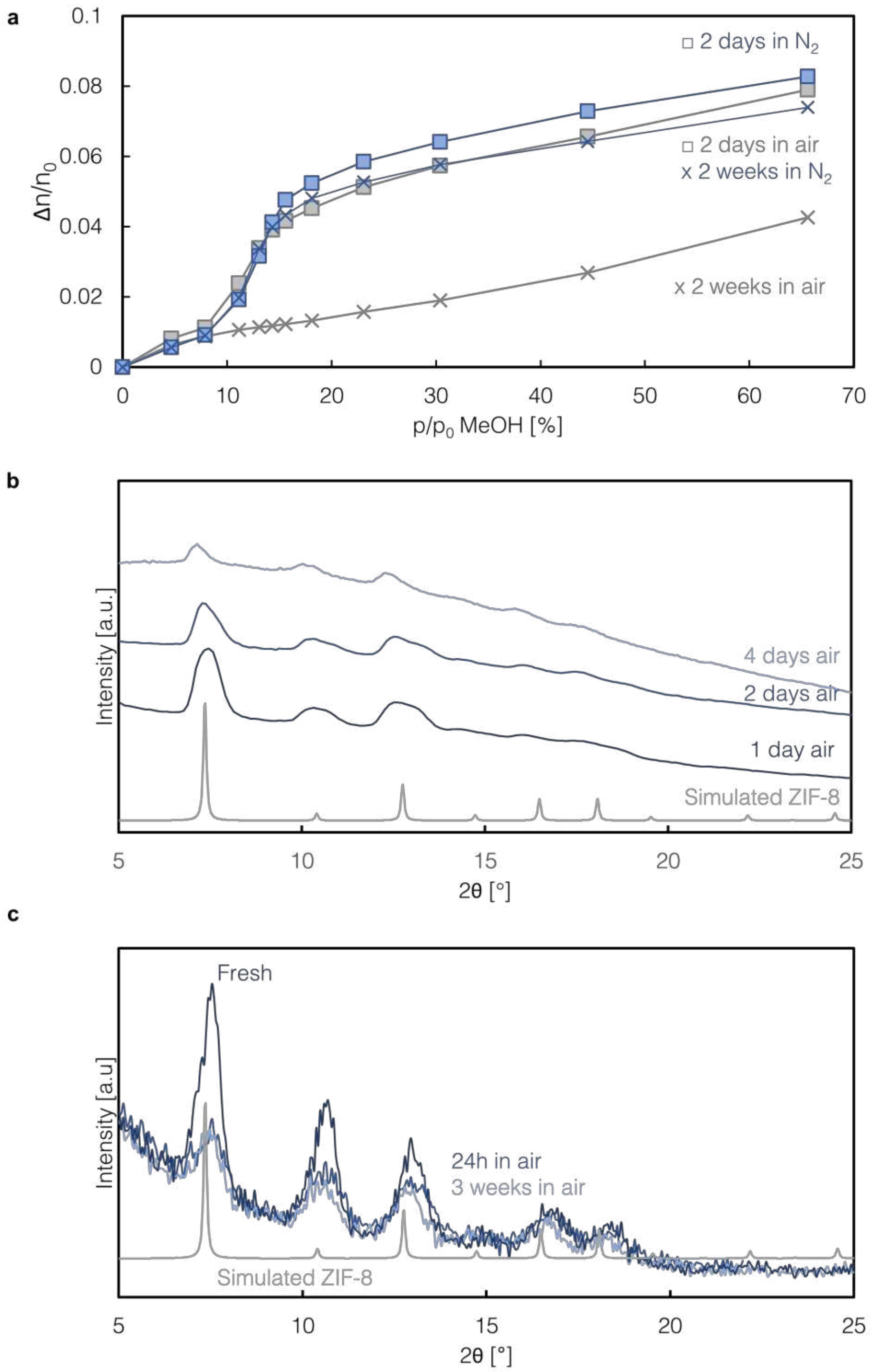

Figure S13 | Study of aging due to exposure to the lab atmosphere with **a)** Ellipsometric porosimetry, all modeled as a Cauchy layer with 10% voids: Decrease in methanol uptake with exposure time to the lab atmosphere. Loss of characteristic S-shaped isotherm at two weeks of air exposure. **b)** Synchrotron GIXRD: decreasing peak intensity with increasing exposure to air. **c)** Lab-based GIXRD: decreasing peak intensity with exposure to air, though at longer exposure times, degradation seems to saturate (*i.e.*, peak intensity stays constant).

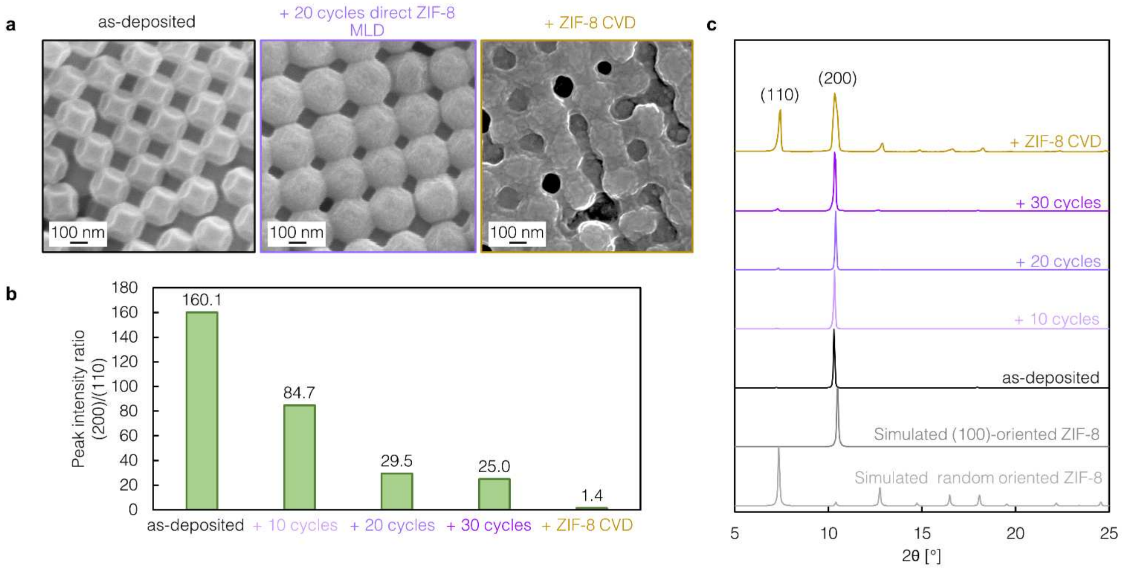

Figure S14 | Direct ZIF-8 MLD on (100) oriented supercrystals. Comparison between bare ZIF-8 supercrystals, supercystals coated with direct ZIF-8 MLD (10, 20, and 30 cycles, 9 Å/cycle), and supercrystals coated with ZIF-8 CVD (from 3 nm ZnO, corresponding to ~30 nm of ZIF-8[2]) a) SEM images b) Peak intensity ratio of (200) peak relative to (110) c) s-XRD patterns normalized to the highest intensity peak.

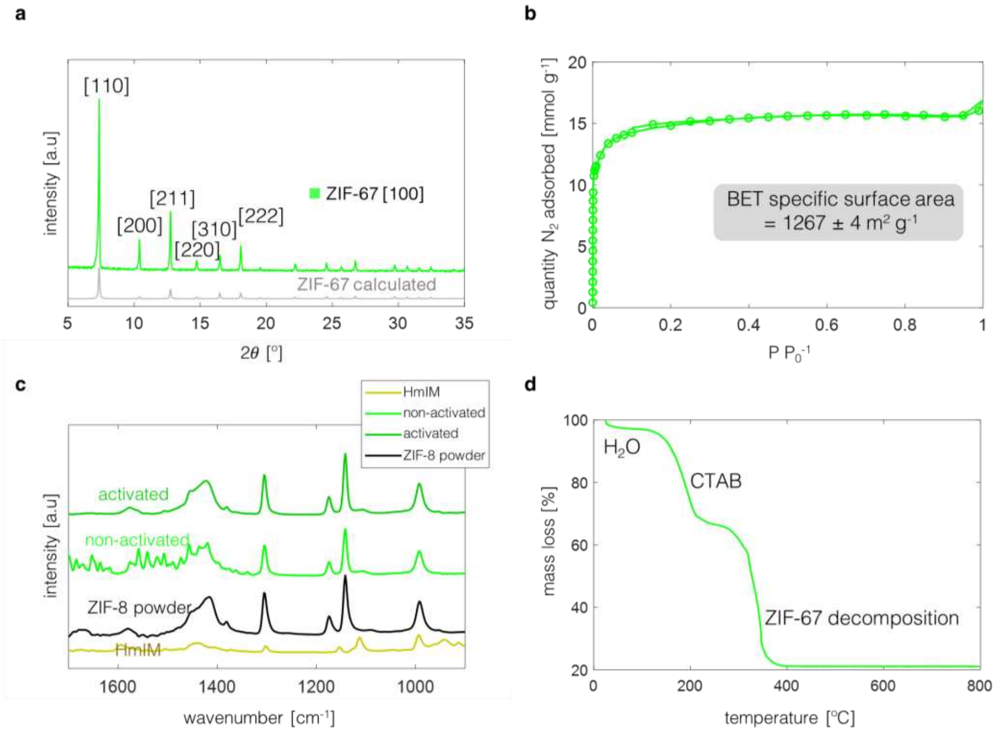

Figure S15 | ZIF-67 crystals powder characterization. a) Powder XRD **b)** N_2 physisorption **c)** ATR-FTIR, and **d)** thermogravimetric analysis of the ZIF-67 crystallites, adapting the method implemented by Avci, *et al*, for ZIF-8.[34] To generate the Co analog of ZIF-8, cobalt acetate $[Co(Ac)_2 \cdot 4\ H_2O]$ was used as the metal precursor instead of a Zn salt[35] (see *Methods*). The FTIR spectra of ZIF-8 powder generated via solution-based synthesis and HmIM powder are included as references. CCDC code for the calculated ZIF-67 diffraction pattern: GITTOT.[36]

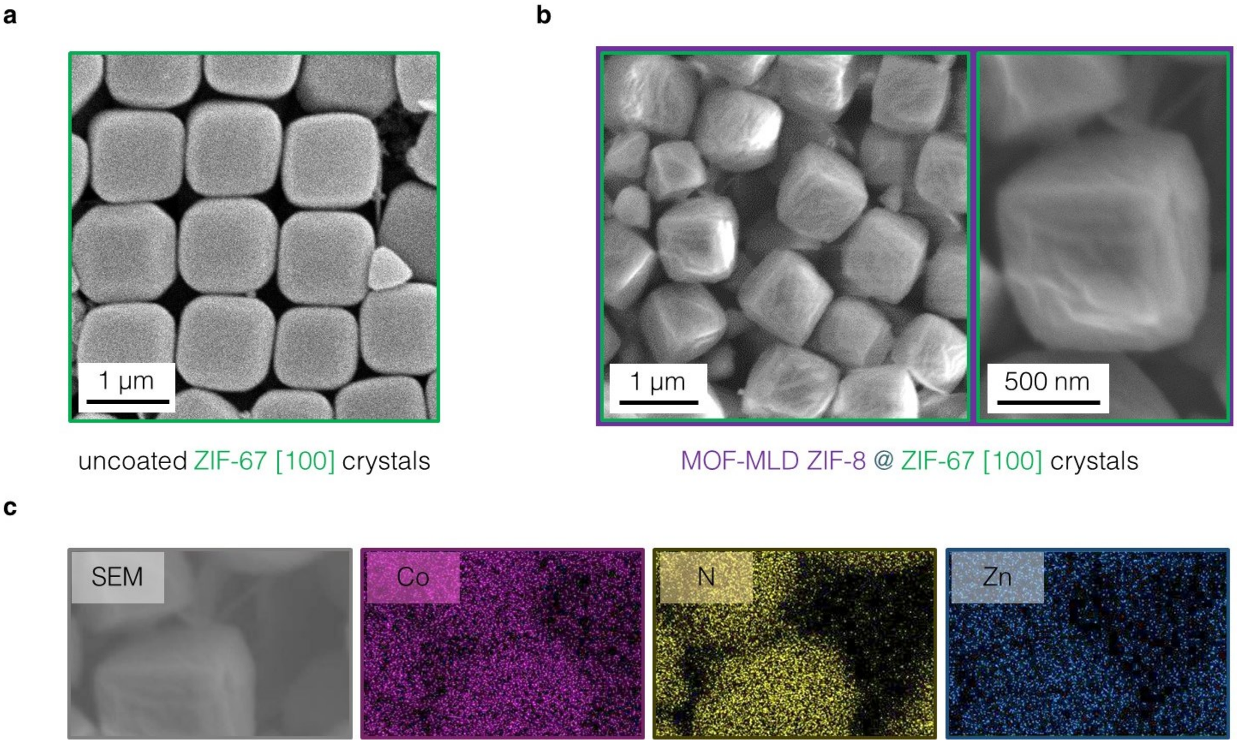

Figure S16 | SEM images ZIF-67 crystals a) before and **b)** after 20 direct ZIF-8 MLD cycles. **c)** Energy-dispersive X-ray spectroscopy (EDX) shows the conformal ZIF-8 (Zn) coating on ZIF-67 (Co).

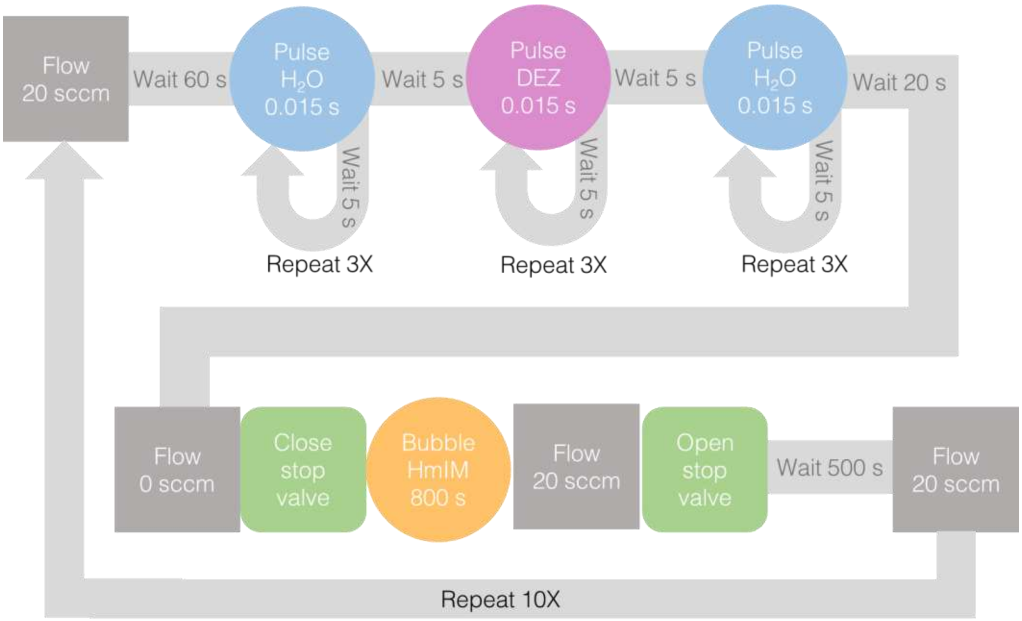

Figure S17 | Direct ZIF-8 MLD schematic representation of the protocol.

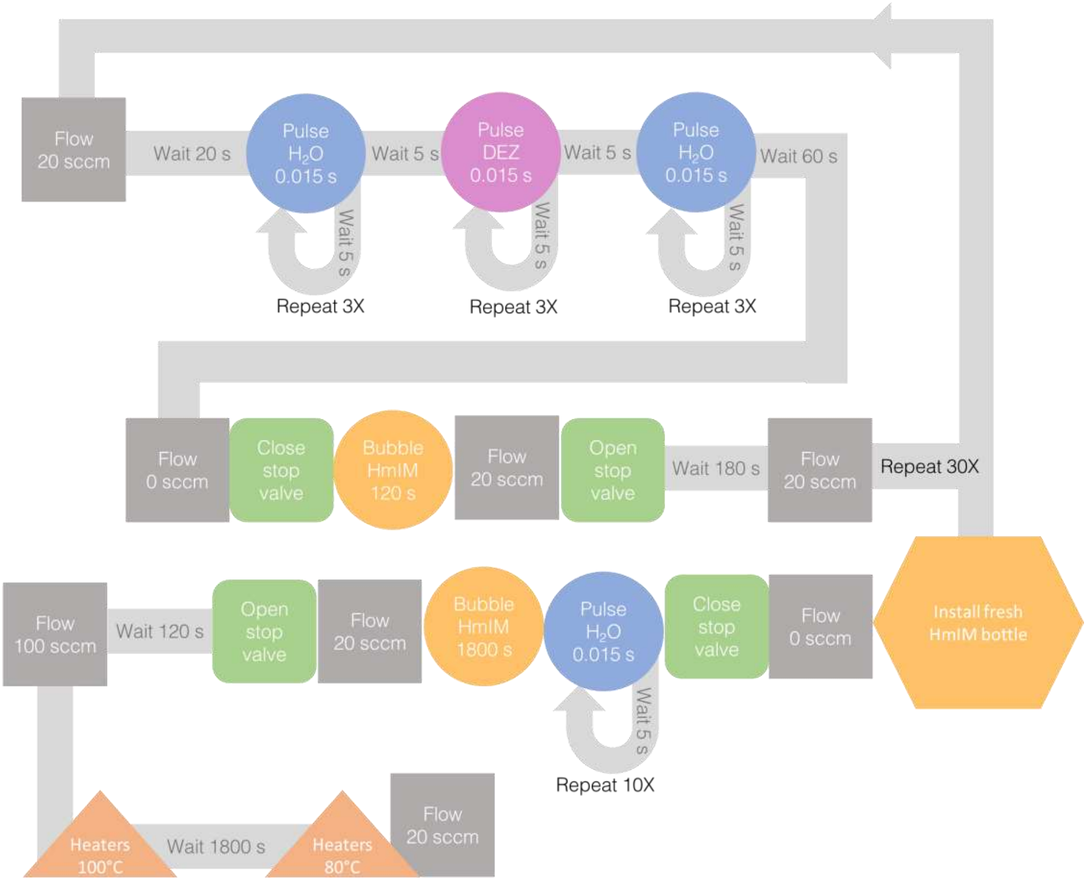

Figure S18 | Two-step ZIF-8 MLD schematic representation of the protocol.

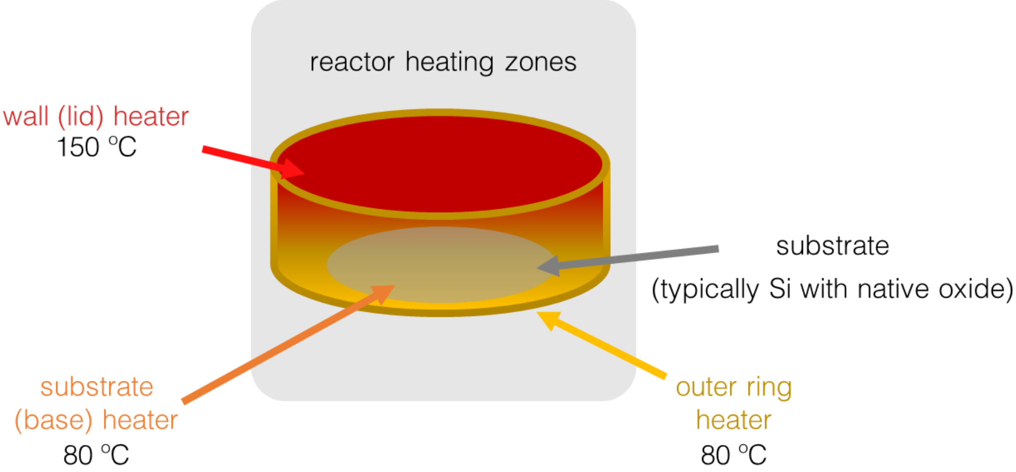

Figure S19 | The optimized temperature gradient in the MOF-MLD reactor. The MOF-MLD chamber has three independently controlled heating zones: the substrate (**1 –** base heater and **2 –** outer ring) and wall (**3** – lid) heaters. These heaters were set to 80 °C (**1, 2**) and 150 °C (**3**), respectively in MOF-MLD. These are the same optimized temperatures for MOF-CVD detailed in our previous work.[2]

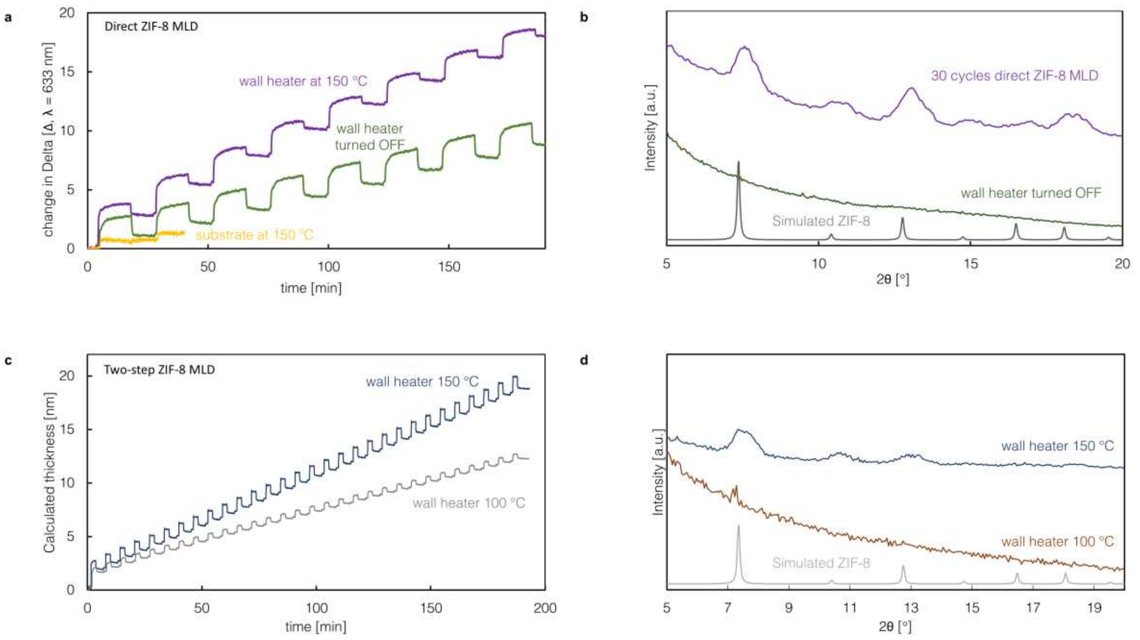

Figure S20 | MOF-MLD optimization of the temperature gradient. a) *in-situ* ellipsometry profiles (change in Delta, at λ = 633 nm) for direct ZIF-8 MLD (purple); the same MLD recipe with the wall heater turned OFF (green, substrate heater at 80 ˚C), and with the wall and substrate heaters set to 150 °C (2 cycles, yellow), with all other process parameters held constant. **b)** GIXRD patterns of direct ZIF-8 MLD (purple) and a sample deposited with the same protocol but with the wall heater turned off (green). **c)** Modelled *in-situ* ellipsometry of the MLD subsection of two-step ZIF-8 MLD. Comparison between wall heater at 150 °C and at 100°C, *i.e.*, a diminishment of the vertical temperature gradient. **d)** GIXRD pattern comparison between two-step ZIF-8 MLD with wall heater at 150 °C and 100 °C. No significant crystallinity was detected with the wall heater at 100 °C.

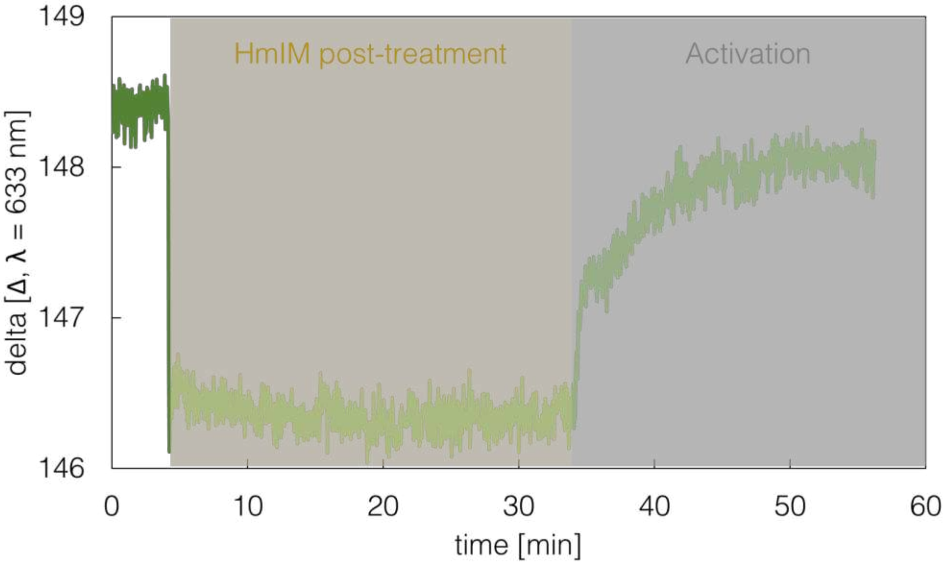

Figure S21 | Ellipsometry of HmIM post-deposition treatment and activation in two-step ZIF-8 MLD. Delta at 633 nm as a function of time.

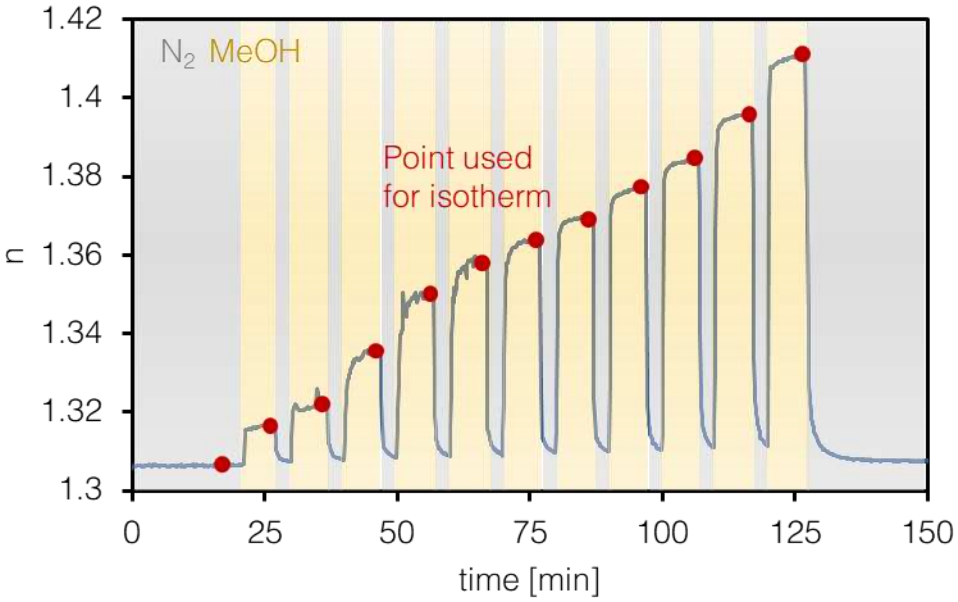

Figure S22 | Ellipsometric porosimetry as a function of time. Two-step ZIF-8 MLD film on Si, where the sample is exposed to eleven different MeOH vapor concentrations separated by inert gas purge streams. Grey areas indicate N_2 purge times, yellow methanol vapor exposure, and red dots indicate the points at which data for the isotherms is exported.

Supporting Information References

(1) Lu, G.; Hupp, J. T. Metal–Organic Frameworks as Sensors: A ZIF-8 Based Fabry–Pérot Device as a Selective Sensor for Chemical Vapors and Gases. *J. Am. Chem. Soc.* **2010**, *132* (23), 7832–7833. https://doi.org/10.1021/ja101415b.

(2) Cruz, A. J.; Stassen, I.; Krishtab, M.; Marcoen, K.; Stassin, T.; Rodríguez-Hermida, S.; Teyssandier, J.; Pletincx, S.; Verbeke, R.; Rubio-Giménez, V.; Tatay, S.; Martí-Gastaldo, C.; Meersschaut, J.; Vereecken, P. M.; De Feyter, S.; Hauffman, T.; Ameloot, R. Integrated Cleanroom Process for the Vapor-Phase Deposition of Large-Area Zeolitic Imidazolate Framework Thin Films. *Chem. Mater.* **2019**, *31* (22), 9462–9471. https://doi.org/10.1021/acs.chemmater.9b03435.

(3) Heinke, L. Diffusion and Photoswitching in Nanoporous Thin Films of Metal-Organic Frameworks. *J. Phys. Appl. Phys.* **2017**, *50* (19), 193004. https://doi.org/10.1088/1361-6463/aa65f8.

(4) Chmelik, C.; Bux, H.; Caro, J.; Heinke, L.; Hibbe, F.; Titze, T.; Kärger, J. Mass Transfer in a Nanoscale Material Enhanced by an Opposing Flux. *Phys. Rev. Lett.* **2010**, *104* (8), 085902. https://doi.org/10.1103/PhysRevLett.104.085902.

(5) Tompkins, H. G.; Hilfiker, J. N. *Spectroscopic Ellipsometry: Practical Application to Thin Film Characterization*; Materials characterization and analysis collection; Momentum Press: New York, NY, 2016.

(6) Horcas, I.; Fernández, R.; Gómez-Rodríguez, J. M.; Colchero, J.; Gómez-Herrero, J.; Baro, A. M. WSXM: A Software for Scanning Probe Microscopy and a Tool for Nanotechnology. *Rev. Sci. Instrum.* **2007**, *78* (1), 013705. https://doi.org/10.1063/1.2432410.

(7) Krywka, C.; Paulus, M.; Sternemann, C.; Volmer, M.; Remhof, A.; Nowak, G.; Nefedov, A.; Pöter, B.; Spiegel, M.; Tolan, M. The New Diffractometer for Surface X-Ray Diffraction at Beamline BL9 of DELTA. *J. Synchrotron Radiat.* **2006**, *13* (1), 8–13. https://doi.org/10.1107/S0909049505035685.

(8) Hammersley, A. P.; Svensson, S. O.; Hanfland, M.; Fitch, A. N.; Hausermann, D. Two-Dimensional Detector Software: From Real Detector to Idealised Image or Two-Theta Scan. *High Press. Res.* **1996**, *14* (4–6), 235–248. https://doi.org/10.1080/08957959608201408.

(9) B, S.; S, P.; M, D.; C, R.; J, D.; T, F.; R, R.; O, W. GIDVis: A Comprehensive Software Tool for Geometry-Independent Grazing-Incidence X-Ray Diffraction Data Analysis and Pole-Figure Calculations. *J. Appl. Crystallogr.* **2019**, *52* (3), 683–689. https://doi.org/10.1107/S1600576719004485.

(10) Tietze, M. L.; Obst, M.; Arnauts, G.; Wauteraerts, N.; Rodríguez-Hermida, S.; Ameloot, R. Parts-per-Million Detection of Volatile Organic Compounds via Surface Plasmon Polaritons and Nanometer-Thick Metal–Organic Framework Films. *ACS Appl. Nano Mater.* **2022**, acsanm.2c00012. https://doi.org/10.1021/acsanm.2c00012.

(11) Trzhaskovskaya, M. B.; Yarzhemsky, V. G. Dirac–Fock Photoionization Parameters for HAXPES Applications. *At. Data Nucl. Data Tables* **2018**, *119*, 99–174. https://doi.org/10.1016/j.adt.2017.04.003.

(12) Avci, C.; Liu, Y.; Pariente, J. A.; Blanco, A.; Lopez, C.; Imaz, I.; Maspoch, D. Template-Free, Surfactant-Mediated Orientation of Self-Assembled Supercrystals of Metal–Organic Framework Particles. *Small* **2019**, *15* (31), 1902520. https://doi.org/10.1002/smll.201902520.

(13) Chen, X.; Oja, V.; Chan, W. G.; Hajaligol, M. R. Vapor Pressure Characterization of Several Phenolics and Polyhydric Compounds by Knudsen Effusion Method. *J. Chem. Eng. Data* **2006**, *51* (2), 386–391. https://doi.org/10.1021/je050293h.

(14) Salmi, L.; Heikkilä, M.; Puukilainen, E.; Sajavaara, T.; Grosso, D.; Ritala, M. Studies on Atomic Layer Deposition of MOF-5 Thin Films. *Microporous Mesoporous Mater.* **2013**, *182*, 147–154. https://doi.org/10.1016/j.micromeso.2013.08.024.

(15) Salmi, L. D.; Heikkilä, M. J.; Vehkamäki, M.; Puukilainen, E.; Ritala, M.; Sajavaara, T. Studies on Atomic Layer Deposition of IRMOF-8 Thin Films. *J. Vac. Sci. Technol. A* **2014**, 33 (1), 01A121. https://doi.org/10.1116/1.4901455.

(16) Ahvenniemi, E.; Karppinen, M. Atomic/Molecular Layer Deposition: A Direct Gas-Phase Route to Crystalline Metal–Organic Framework Thin Films. *Chem. Commun.* **2016**, 52 (6), 1139–1142. https://doi.org/10.1039/C5CC08538A.

(17) Multia, J.; Kravchenko, D. E.; Rubio-Giménez, V.; Philip, A.; Ameloot, R.; Karppinen, M. Nanoporous Metal–Organic Framework Thin Films Prepared Directly from Gaseous Precursors by Atomic and Molecular Layer Deposition: Implications for Microelectronics. *ACS Appl. Nano Mater.* **2023**, 6 (2), 827–831. https://doi.org/10.1021/acsanm.2c04934.

(18) Medishetty, R.; Zhang, Z.; Sadlo, A.; Cwik, S.; Peeters, D.; Henke, S.; Mangayarkarasi, N.; Devi, A. Fabrication of Zinc-Dicarboxylate- and Zinc-Pyrazolate-Carboxylate-Framework Thin Films through Vapour-Solid Deposition. *Dalton Trans.* **2018**, 47 (40), 14179–14183. https://doi.org/10.1039/C8DT00352A.

(19) Ahvenniemi, E.; Karppinen, M. In Situ Atomic/Molecular Layer-by-Layer Deposition of Inorganic–Organic Coordination Network Thin Films from Gaseous Precursors. *Chem. Mater.* **2016**, 28 (17), 6260–6265. https://doi.org/10.1021/acs.chemmater.6b02496.

(20) Lausund, K. B.; Nilsen, O. All-Gas-Phase Synthesis of UiO-66 through Modulated Atomic Layer Deposition. *Nat. Commun.* **2016**, 7 (1). https://doi.org/10.1038/ncomms13578.

(21) Lausund, K. B.; Petrovic, V.; Nilsen, O. All-Gas-Phase Synthesis of Amino-Functionalized UiO-66 Thin Films. *Dalton Trans.* **2017**, 46 (48), 16983–16992. https://doi.org/10.1039/C7DT03518G.

(22) Lausund, K. B.; Olsen, M. S.; Hansen, P.-A.; Valen, H.; Nilsen, O. MOF Thin Films with Bi-Aromatic Linkers Grown by Molecular Layer Deposition. *J. Mater. Chem. A* **2020**, 8 (5), 2539–2548. https://doi.org/10.1039/C9TA09303F.

(23) Tanskanen, A.; Karppinen, M. Iron-Terephthalate Coordination Network Thin Films Through In-Situ Atomic/Molecular Layer Deposition. *Sci. Rep.* **2018**, 8 (1), 8976. https://doi.org/10.1038/s41598-018-27124-7.

(24) Han, S.; Ciufo, R. A.; Meyerson, M. L.; Keitz, B. K.; Mullins, C. B. Solvent-Free Vacuum Growth of Oriented HKUST-1 Thin Films. *J. Mater. Chem. A* **2019**, 7 (33), 19396–19406. https://doi.org/10.1039/C9TA05179A.

(25) Khayyami, A.; Philip, A.; Karppinen, M. Atomic/Molecular Layer Deposited Iron–Azobenzene Framework Thin Films for Stimuli-Induced Gas Molecule Capture/Release. *Angew. Chem. Int. Ed.* **2019**, 58 (38), 13400–13404. https://doi.org/10.1002/anie.201908164.

(26) Silva, R. M.; Carlos, L. D.; Rocha, J.; Silva, R. F. Luminescent Thin Films of Eu-Bearing UiO-66 Metal Organic Framework Prepared by ALD/MLD. *Appl. Surf. Sci.* **2020**, 527, 146603. https://doi.org/10.1016/j.apsusc.2020.146603.

(27) Yase, K.; Takahashi, Y.; Ara-kato, N.; Kawazu, A. Evaporation Rate and Saturated Vapor Pressure of Functional Organic Materials. *Jpn. J. Appl. Phys.* **1995**, 34 (2R), 636. https://doi.org/10.1143/JJAP.34.636.

(28) Wakayama, N.; Inokuchi, H. Heats of Sublimation of Polycyclic Aromatic Hydrocarbons and Their Molecular Packings. *Bull. Chem. Soc. Jpn.* **1967**, 40 (10), 2267–2271. https://doi.org/10.1246/bcsj.40.2267.

(29) Niskanen, A.; Hatanpää, T.; Ritala, M.; Leskelä, M. Thermogravimetric Study of Volatile Precursors For Chemical Thin Film Deposition. Estimation of Vapor Pressures and Source Temperatures. *J. Therm. Anal. Calorim.* **2001**, 64 (3), 955–964. https://doi.org/10.1023/A:1011579114687.

(30) Ribeiro da Silva, M. A. V.; Monte, M. J. S.; Santos, L. M. N. B. F. The Design, Construction, and Testing of a New Knudsen Effusion Apparatus. *J. Chem. Thermodyn.* **2006**, 38 (6), 778–787. https://doi.org/10.1016/j.jct.2005.08.013.

(31) *Handbook of Thermal Analysis and Calorimetry: Recent Advances, Techniques and Applications*; Elsevier: Amsterdam, The Netherlands, 2018.

(32) Jiménez, P.; Roux, M. V.; Turrión, C. Thermochemical Properties of N-Heterocyclic Compounds IV. Enthalpies of Combustion, Vapour Pressures and Enthalpies of Sublimation, and Enthalpies of Formation of 2-Methylimidazole and 2-Ethylimidazole. *J. Chem. Thermodyn.* **1992**, 24 (11), 1145–1149. https://doi.org/10.1016/S0021-9614(05)80237-X.

(33) Almeida, A. R. R. P.; Monte, M. J. S. Thermodynamic Study of Phase Transitions of Imidazoles and 1-Methylimidazoles. *J. Chem. Thermodyn.* **2012**, 44 (1), 163–168. https://doi.org/10.1016/j.jct.2011.08.017.

(34) Avci, C.; Liu, Y.; Pariente, J. A.; Blanco, A.; Lopez, C.; Imaz, I.; Maspoch, D. Template-Free, Surfactant-Mediated Orientation of Self-Assembled Supercrystals of Metal–Organic Framework Particles. *Small* **2019**, *15* (31), 1902520. https://doi.org/10.1002/smll.201902520.

(35) Qian, J.; Sun, F.; Qin, L. Hydrothermal Synthesis of Zeolitic Imidazolate Framework-67 (ZIF-67) Nanocrystals. *Mater. Lett.* **2012**, 82, 220–223. https://doi.org/10.1016/j.matlet.2012.05.077.

(36) Banerjee, R.; Phan, Anh; Wang, Bo; Knobler, C.; Furukawa, H.; O'Keeffe, M.; Yaghi, O.M. CCDC 671073: Experimental Crystal Structure Determination, 2008. https://doi.org/10.5517/CCQJ9J1.